Study of Cross-flow Cooling Effects in a Stirling Engine Heat Exchanger

by

Erin Eppard

A Thesis Presented in Partial Fulfillment
of the Requirements for the Degree
Master of Science

Approved November 2011 by the
Graduate Supervisory Committee:

Patrick Phelan, Chair
Steven Trimble
Ronald Calhoun

ARIZONA STATE UNIVERSITY

December 2011

ABSTRACT

While much effort in Stirling engine development is placed on making the high-temperature region of the Stirling engine warmer, this research explores methods to lower the temperature of the cold region by improving heat transfer in the cooler.

This paper presents heat transfer coefficients obtained for a Stirling engine heat exchanger with oscillatory flow. The effects of oscillating frequency and input heat rate on the heat transfer coefficients are evaluated and details on the design and development of the heat exchanger test apparatus are also explained.

Featured results include the relationship between overall heat transfer coefficients and oscillation frequency which increase from 21.5 to 46.1 $Wm^{-2}K^{-1}$ as the oscillation frequency increases from 6.0 to 19.3 Hz. A correlation for the Nusselt number on the inside of the heat exchange tubes in oscillatory flow is presented in a concise, dimensionless form in terms of the kinetic Reynolds number as a result of a statistical analysis. The test apparatus design is proven to be successful throughout its implementation due to the usefulness of data and clear trends observed.

The author is not aware of any other publicly-available research on a Stirling engine cooler to the extent presented in this paper. Therefore, the present results are analyzed on a part-by-part basis and compared to segments of other research; however, strong correlations with data from other studies are not expected.

The data presented in this paper are part of a continuing effort to better understand heat transfer properties in Stirling engines as well as other oscillating flow applications.

ACKNOWLEDGMENTS

TABLE OF CONTENTS

LIST OF TABLES

LIST OF FIGURES

NOMENCLATURE

A	Area [m^2]	
A_ω	Dimensionless oscillation amplitude [$-$]	
C	Correlation coefficient [$-$]	
c_p	Specific heat at constant pressure [kJ kg^{-1} K^{-1}]	
d	Diameter of the tube [m]	
δ	Finite increment in a value [$-$]	
ΔP	Finite increment in pressure [kPa]	
ΔT	Finite increment in temperature [°C]	
f	Frequency [Hz]	
h	Heat transfer coefficient [W m^{-2} K]	
η	Thermal efficiency [$-$]	
k	Thermal conductivity [W m^{-1} K^{-1}]	
L	Tube length [m]	
l	Tube wall thickness [m]	
m	Mass [kg]	
μ	Dynamic viscosity [kg s^{-1} m^{-1}]	
Nu	Nusselt number [$-$]	
Pr	Prandtl number [$-$]	
p_t	Transverse tube pitch [m]	
ρ	Density [kg m^{-3}]	
$\dot{Q}$	Total heat transfer [W]	
$\dot{q}$	Heat flux [W m^{-2}]	
Re	Reynolds number [$-$]	
Re_ω	Dimensionless oscillation frequency [$-$]	
S_l	Dimensionless longitudinal tube pitch [$-$]	
S_t	Dimensionless transverse tube pitch [$-$]	
T	Temperature [°C]	
θ	Angle of tube staggering [deg]	
U	Overall heat transfer coefficient [W m^{-2} K]	
u	Velocity [m s^{-1}]	
V	Volume [m^3]	
ν	Kinematic viscosity [m^2 s^{-1}]	
$\dot{W}$	Power [W]	
ω	Oscillatory frequency [rad s^{-1}]	
X_l	Longitudinal tube pitch [$-$]	
X_t	Transverse tube pitch [$-$]	
x_{max}	Maximum amplitude of working fluid displacement [m]	

Subscripts

1	State one
2	State two
a	Air (working fluid)
av	Average
c	Cold
$Carn$	Carnot
$cond$	Conduction
$conv$	Convection
f	Cross-sectional, frontal, free-flow
h	Hot
hyd	Hydraulic
i	Inside/inner
lm	Logarithmic mean
m	Mean value
max	Maximum
o	Outside/outer
$overall$	Overall
s	Heater (heat source)
W	Wall
w	Water (coolant)

Superscripts

$\cdot$	Time rate of change

PREFACE

Since the research presented in this paper is the culmination of both an undergraduate honors thesis as well as a Master's thesis, it is important to distinguish the more recent work from the older work. There is no overlap of data between the undergraduate and Master's thesis work. All data presented in this paper have been specifically acquired to study the effects of cross-flow on heat exchange at four different heat rates and five different oscillation frequencies. New discoveries in this paper include the validation that the overall heat transfer coefficient continues to increase as frequency is increased over a wider range of frequencies. Some of the most significant changes to the test apparatus between the undergraduate and Master's thesis work include the implementation of isolator devices designed to prevent airborne contaminants from the compressor pump from fouling the heat exchange surfaces on the inside of the tube bundle and a mechanical diverter ("filler material") that prevents coolant flow in areas not of interest, such as around the perimeter of the tube bundle, rather than through the tube bundle. Both of these changes were considered necessary after a review of data from the author's undergraduate thesis. Other modifications include the implementation of a DC motor to allow for precisely-controlled speeds that reach the lower bound of speeds used in Stirling engines, a more controlled siphoning technique for the coolant, and numerous measures taken to ensure the minimization of unwanted heat sources having an impact on the data [1], [2]. One of the methods of isolating unwanted heat sources includes the use of a plastic isolator coupling to break a major path of thermal conduction through the shell of the heat exchanger. It is suggested that the reader briefly review the schematic shown in Fig. 2.1 and 2.13 for an overview of the physical setup of the experiment before proceeding with reading the rest of the manuscript.

Also, due to the unique experiments that were preformed, any correlations made to other researcher's works will have to be prefaced by a lengthy explanation of the difference in physical setups between the experiments. Strong correlations with other research are not expected due to different heat exchanger geometries and test rig configurations.

Chapter 1: INTRODUCTION

While extensive effort in Stirling engine research is focused on improving heat exchange in the higher-temperature regions of the Stirling engine, this research gives more insight to heat exchange that occurs on the low-temperature side of the engine. Initially, by inspection of the Carnot equation for the ideal heat engine efficiency, it can be seen that reducing the low temperature by one unit yields a larger improvement to the overall thermal efficiency than raising the high temperature by the same amount in (1):

$$\eta_{Carn} = 1 - \frac{T_c}{T_h} \tag{1}$$

where η_{Carn} is the Carnot efficiency, T_c the coldest temperature, and T_h the warmest temperature in the engine. The same case should hold true in the present analysis: improvements to the heat exchanger efficiency on the cold side of the engine should yield a better overall thermal efficiency than making improvements to the heat exchanger on the warm side of the engine. Despite this, research on Stirling regenerators and heaters far outweighs research on coolers. In fact, one of the most-studied components in the Stirling engine is the regenerator, for which there are complete books dedicated to the subject [3]. However, this is justified since the majority of improvements to heat transfer are dependent on the regenerator. A good indication of this is that 70–90% of the pressure drop across all components in the Stirling engine occurs in the regenerator and larger pressure drops are correlated with more efficient heat transfer [4].

When the cooler is evaluated independently of the other Stirling engine components in an analytical model for a Space Power Research Engine (SPRE), it was found that a 25% reduction in the effectiveness of the cooler reduced the overall engine thermal efficiency by only 2%, whereas a 1.8% reduction in the effectiveness of the regenerator reduced the overall engine thermal efficiency by 12.2% [5], [6]. The impact of the cooler on the overall engine thermal efficiency is slightly less than that of the heater, where a 46% reduction in the effectiveness of the heater would reduce the overall engine thermal efficiency by 4.1% [5], [6]. The effectiveness of the heat exchangers is best described as the ratio between the measured heat transfer rate and maximum attainable heat transfer rate which would be realized in a counterflow heat exchanger with

unlimited area for heat exchange [7]. This further emphasizes that if the effectiveness of the heater and cooler are equally weighted in the calculation of the overall thermal efficiency, then more research efforts should be dedicated to improving the cooler to balance the amount of research that has been performed on the heater.

Oscillating flow heat transfer adds significant complexity to the analysis of Stirling engine heat transfer. In fact, within the field of oscillatory flow heat transfer, consensus has not been reached on whether oscillations improve or reduce the heat transfer coefficients [8]. What is known, however, is that transition to the turbulent flow regime occurs at higher values of the maximum Reynolds number when the kinetic Reynolds number increases where the Reynolds number is defined as [9]:

$$Re = \frac{\rho \, u \, d}{\mu} \tag{2}$$

and the kinetic Reynolds number is defined as [9]:

$$Re_\omega = \frac{\omega \, d^2}{\nu} \tag{3}$$

where ρ is the density, u the velocity, d the diameter, μ the dynamic viscosity, ω the angular oscillatory frequency, and ν the kinematic viscosity.

1.1. OBJECTIVES

Experimental data are required for the present analysis since there are few published expressions which correlate the overall heat transfer coefficient with different heat exchange parameters in oscillating flows. Therefore, a test apparatus was designed in order to collect data on this unique type of heat transfer in Stirling engines. The main objectives for this study were to: 1) build an adaptable Stirling engine cooler test apparatus capable of obtaining data with minimal error; 2) present experimental data for a shell and tube heat exchanger with oscillatory air flow; 3) determine overall heat transfer coefficients; 4) present results in terms of similarity parameters which can be scaled to other research; and 5) briefly compare results to other research.

The foundation for this research is based on the scarcity of data relating performance characteristics to oscillatory flow heat exchangers when compared to uni-directional flow heat exchangers. This paper will not address the issue of whether oscillating flow yields better heat transfer than an equivalent unidirectional flow, nor will it correlate the performance of uni-directional flows to the performance expected by an equivalent oscillatory flow. This is because the results of these experiments are intended to apply to Stirling engine heat exchangers which, by nature of their closed cycle, are required to use oscillating flow. In most of the applications of oscillating flows, unidirectional flows are simply not an option due to the thermodynamic cycle or physical configuration.

1.2. HEAT EXCHANGER

The present experiments were performed on a shell-and-tube heat exchanger subject to oscillating flow on the inside of the tube bundle and transverse, unidirectional water flow over the outside of the tubes in the tube bundle. Fig. 1.1 represents the cross-flow arrangement of coolant flow over the tube bundle (since coolant flows transversely over the tube bank).
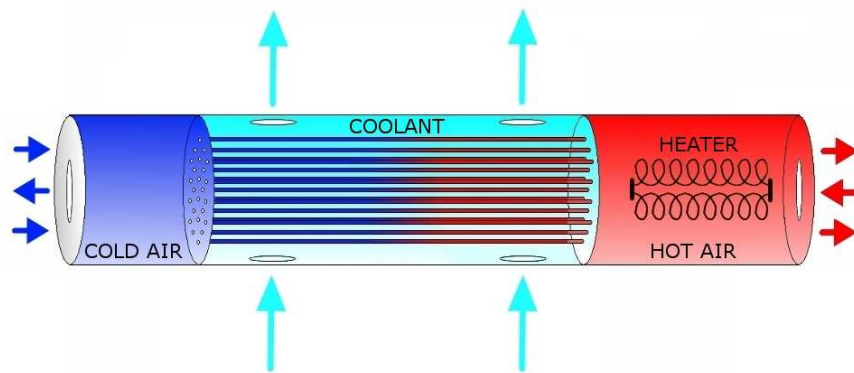
Fig. 1.1. Representation of a cross-flow shell and tube heat exchanger

In Fig. 1.1, the side of the cooler with the heater element is often referred to in this paper as the "hot side" and the opposite side with cold gas as the "cold side". Air is alternately heated and cooled in each cycle as it flows over the heater element and is subsequently cooled by the coolant

flowing over the tubes in the tube bundle. This process is shown in Fig. 1.2 as indicated by the
direction and color of the arrows during the first and second halves of the cycle.
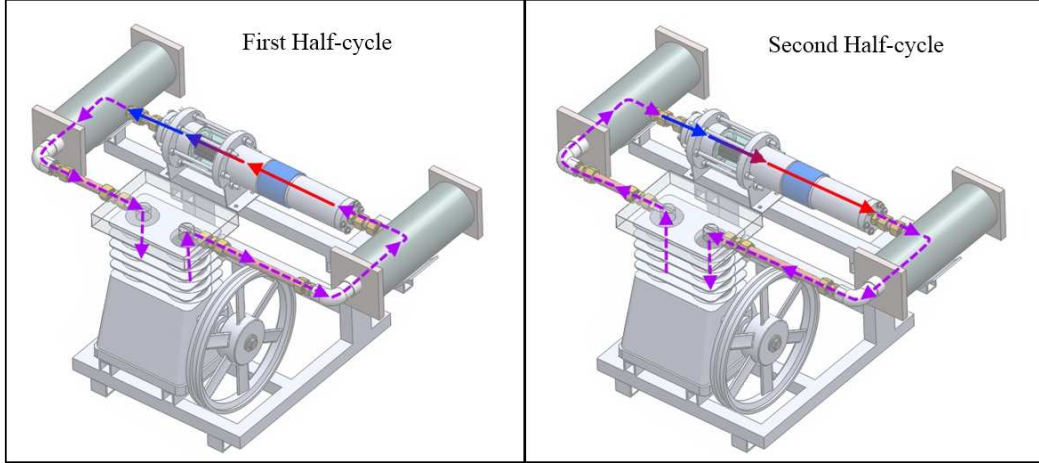
Fig. 1.2. Air flow path during heating and cooling

For air, the factors involved in the calculation of the transition to turbulent flow are the
dimensionless oscillation amplitude, A_ω, and the kinetic Reynolds number, Re_ω [8]. These factors
are combined in (4) to indicate the transition point from laminar to turbulent flow in oscillatory
flows [8]:

$$A_\omega \sqrt{Re_\omega} > 761 \tag{4}$$

where the dimensionless oscillation amplitude is defined as [8]:

$$A_\omega = \frac{x_{max}}{d_i} \tag{5}$$

where x_{max} is the maximum amplitude of working fluid displacement (assuming plug flow) and
d_i the inner diameter of the tubes [10]. From the definition given in (4), the data collected in the
present experiment is considered to be in the transitional and turbulent flow regime; however,
there is some uncertainly in how to define the dimensionless oscillation amplitude for the present
experiment, which would affect the results obtained from (4). This is because a variety of
definitions have been used for the dimensionless oscillation amplitude. For example, X. Tang and

P. Cheng and T. W. Simon and J. R. Seume define the dimensionless oscillation amplitude as [11], [9]:

$$A_\omega = \frac{x_{max}}{L} \tag{6}$$

where L is the tube length. The definitions of the dimensionless oscillation amplitude given in both (5) and (6) are intended to give a measure of the amount of working fluid displacement [9]. Higher dimensionless oscillation amplitudes indicate that a larger cold volume of air was displaced through the heat exchanger during each half-cycle which corresponds to a drop in the tube wall temperature [10]. Another physical meaning of the dimensionless oscillation amplitude defined in (6) is whether the oscillating fluid exits the tube during each half-cycle, or whether the working fluid continually oscillates inside the tube due to a small piston stroke length as studied by A. J. Organ [12], [9]. Organ found that when $A_\omega = 1$ all of the working fluid passes through the heat exchanger whereas when $A_\omega > 1$ (as in the present research) the fluid passes through the heat exchanger while the remainder of the fluid oscillates inside the heat exchanger without leaving [12], [9]. Once again addressing the point of transition to turbulent flow given by T. Zhao and P. Cheng in (4), if the dimensionless oscillation amplitude is defined as in (5), A_ω would be 1129, whereas if is defined as in (6), A_ω would only be 10.7 [8]. To keep in accordance with the way T. S. Zhao and P. Cheng define A_ω in (4), the dimensionless oscillation amplitude will be taken as 1129 and thus, the air is considered to be in the transitional and turbulent flow regimes [10].

1.3. THE STIRLING ENGINE

It is important to clarify that the test rig constructed for this research is not intended to be used as, or part of, a Stirling engine. In a Stirling engine, the heat provided to the working fluid is sufficient to expand the working fluid and produce enough force to drive the pistons, whereas in this experiment, heat is applied to the gas but the pistons are powered by a separate motor in order to simulate the working environment of a cooler in a Stirling engine. The test rig was built to conduct heat transfer experiments on an isolated Stirling engine cooler. While in use, the Stirling

engine cooler is a robust device and often one of the most expensive components in the engine as reported for Phase I of an automotive Stirling engine where the four coolers attributed for 27.7% of the cost for the entire Stirling engine [13]. Still, in other Stirling engines, the cooler cost has been reported to be as low as 2.2% of the total cost of the engine, such as in the Mod II automotive Stirling engine design [13]. In a typical Stirling engine cooler, helium or hydrogen gas oscillates within the cooler tubes at rates up to about 60 Hz (3600 RPM) [13], [14].

1.4. RELATION TO OTHER RESEARCH

The scale of the heat exchange tubes in the present research is the smallest scale that has been studied in oscillating flow, as far as the author is aware, with the exception of research performed on a single tube in oscillatory flow by P. Bouvier *et al*. [15]. The tubes are nearly the same size as those in other Stirling engine coolers, such as the STM 4-120 Stirling engine cooler; however, research on oscillating flow is typically performed on a single tube while only considering one or two thermal resistances [11], [10]. The small diameter of the tubes in the tube bank result in a very large value of the dimensionless fluid displacement, $A_\omega = 1129$, when compared with typical values between 8 and 35 reported in other research [10].

Many other researchers in the field of oscillating flow perform analyses on tubes with a constant heat flux imposed on the outer tube walls [15], [10]. The calculations corresponding to their analysis assume a constant heat flux through the tube walls and almost always require known values of the tube wall temperature [15], [10]. In the present experiment, the small size of the capillary tubes in the tube bundle made it such that the tube wall temperature could not be measured. It was not considered worthwhile to attempt inserting thermocouples with a diameter of 7.62×10^{-5} m (0.003 in) into a tube wall that was 4.32×10^{-4} m (0.017 in) thick. Machining on such a small scale was not within the capability of the author.

Due to the lack of a comprehensive algorithm for determining the heat transfer coefficients in a heat exchanger involving multiple modes of heat exchange, different analytical equations and correlations will be used to determine heat transfer coefficients corresponding to each of the resistances as shown in Fig. 1.3.

Convection from the
air to the tube wall

Conduction through
the tube wall

Convection from the
tube wall to the water

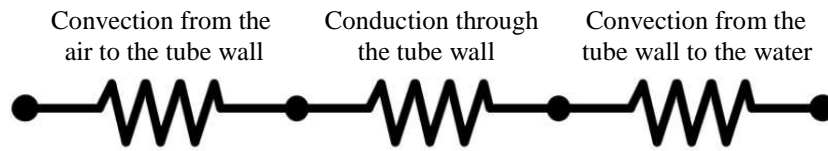Fig. 1.3. Diagram of thermal resistances in the shell and tube heat exchanger

Each resistance in Fig. 1.3 will be analyzed separately and will involve different analytical

methods for its calculation. Note that the resistances can be thought of as the inverse heat transfer

coefficients for each mode of heat transfer and will add together in a parallel resistance fashion to

yield an overall, equivalent resistance.

Chapter 2: APPROACH

In order to study the unique working environment of a Stirling engine cooler, a custom test apparatus needed to be designed and built. The most important objectives that were considered while designing the test apparatus were to: 1) simulate, as best as possible, the working environment of a Stirling engine; 2) establish controls in the experiment and design for minimization of error in data acquisition; and 3) obtain data that accommodate all of the parameters needed in the equations for analysis. Each of these factors will be discussed in the following sections. Fig. 2.1 indicates all ports in the heat exchanger test apparatus which are used either for air flow, water flow, or instrumentation.
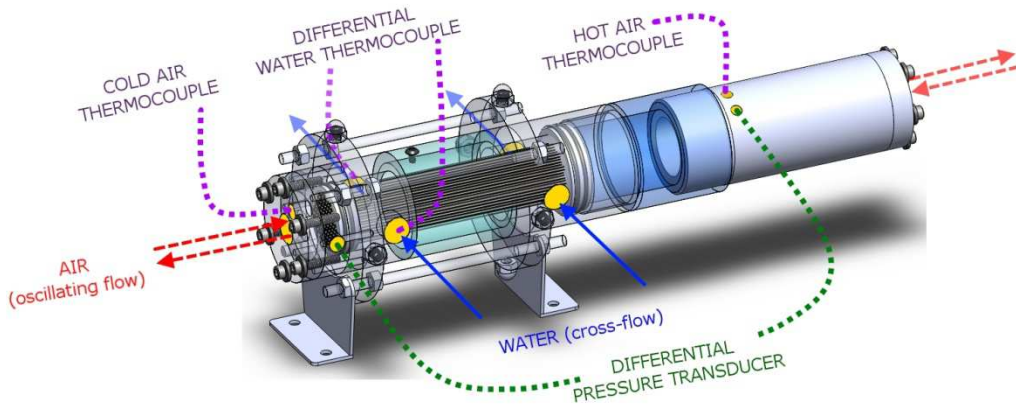
Fig. 2.1. Diagram of ports included in the heat exchanger test apparatus

Justification for the location of each data acquisition port and the overall design of the heat exchanger test apparatus will be discussed in detail in later sections of this paper.

2.1. DESIGN OF HEAT EXCHANGER EXPERIMENT

Of primary importance when designing the test apparatus was the minimization of error while still producing a relatively inexpensive unit that was safe, portable, and capable of simulating the working conditions of a Stirling engine. Due to the safety and financial concerns of pressurizing warm air within the test apparatus, it was decided to simply measure the pressure

drop across the tube bank (using the differential pressure transducer ports shown in Fig. 2.1) and assume that the pressure inside the test apparatus is equal to ambient pressure. This assumption was eventually verified by machining an access port into the heat exchanger and connecting a pressure gage to the port. When the compressor pump in the test apparatus was activated, the pressure gage was unaffected by the pressures due to both the gage pressure and the pressure drop across the tube bundle. Therefore, the combination of these pressures did not exceed the 34.5 kPa sensitivity of the pressure gauge, and pressures below this level were assumed to have a negligible effect on heat exchange.

2.1.1. DESIGN OF HEAT EXCHANGER

There is a wide array of configurations for Stirling engine coolers. Some configurations feature an annular cooler that fits concentrically around the piston cylinder and is cooled by coolant in cross-flow, such as in the NASA/MTI Automotive Stirling Engine and the SPRE engine [13], [6]. Still others incorporate coolant that travels parallel to the cooling tubes in the cooler, such as with the Sunpower RE-1000 Stirling engine [6]. Most commonly, the coolant passes transversely over the tubes in the cooler, as represented in the STM 4-120 Stirling engine. The fabricated cooler was designed to resemble an actual Stirling engine cooler from a STM 4-120 engine as shown in Fig. 2.2.

Fig. 2.2. Comparison of the fabricated cooler (left) to an STM 4-120 cooler (right)

The stainless steel tubes in the fabricated heat exchanger are positioned in aluminum perforated end caps held together and sealed with high-temperature and water resistant Loctite® adhesive whereas the STM 4-120 cooler has a stainless steel construction which is brazed together. The tube bundle in the fabricated heat exchanger is composed of stainless steel tubes since it is a common choice for Stirling engine cooler tubes. This is most likely due to the moderate conductivity of stainless steel with respect to other metals which allows for a trade-off between radial (desired) and longitudinal (un-desired) wall conduction. After all, one of the primary functions of the cooler is to produce a measureable temperature gradient at the cold end of the Stirling engine.

Tube bundle geometries are commonly reported in terms of the dimensions shown in Fig. 2.3 [16].
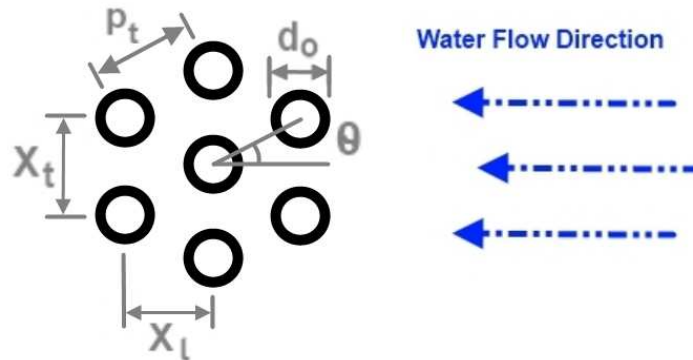
Fig. 2.3. Dimensions of the staggered tube bank (adapted from [16])

These dimensions are important for similarity and scaling between experiments on different heat exchangers and may be found commonly reported in literature [16]. The corresponding dimensions in Fig. 2.3 are listed in Table 2.1 along with the dimensions of the STM 4-120 cooler (dimensions of the STM 4-120 cooler were measured directly by the author).

Table 2.1. Dimensions of the fabricated cooler and STM 4-120 cooler [16]

	Fabricated Cooler	STM 4-120 Cooler
Outside diameter, d_o (mm)	2.11	2.38
Angle of tube staggering, θ	60	60
Transverse tube pitch, $X_t = p_t$ (mm)	3.16	2.89
Longitudinal tube pitch, X_l (mm)	2.74	2.50

A condensed list of the geometric properties and fluids used in the fabricated cooler and the STM 4-120 are included in Table 2.2 for comparison. Both heat exchangers are made from similar metals and have staggered tube banks [14].

11

Table 2.2. Specifications of the fabricated cooler and STM 4-120 cooler [14]

	Fabricated Cooler	STM 4-120 Cooler
Number of tubes	97	395
Tube length (mm)	131.4	62.4
Tube inner diameter (mm)	1.25	1.37
Tube outer diameter (mm)	2.11	2.38
Equi-distant tube spacing (mm)	3.16	2.89
Average heat transfer area (mm^2)	$\approx 67\,100$	$\approx 145\,000$
Hot fluid	Air	Hydrogen gas
Max. temperature (°C)	87.3	739
Min. temperature (°C)	38.2	-
Average cycle pressure (Pa)	≈ 0	13 850 000
Volume displaced (mm^3)	165 900	120 000
Cold fluid	Water	50/50 water and glycol [17]
Max temperature (°C)	44.9	56
Min temperature (°C)	19.5	50
Volumetric flow rate (m^{3}s^{-1})	2.19×10^{-6}	2.60×10^{-3}
Ambient temperature (°C)	21	44
Average Oscillation Frequency (Hz)	9.0	30

Some of the most notable differences between the fabricated cooler and the STM 4-120 cooler in Table 2.2 are the differences in average heat transfer area and volumetric flow rate of air [17], [14]. The heat transfer area in the fabricated cooler is 46.3% of the heat exchange surface area in the STM 4-120 cooler [17]. Also, the equi-distant tube spacing is more than four times greater than that of the STM 4-120 cooler. This results in a lower heat transfer coefficient on the outside of the tube bundle since the STM 4-120 cooler will yield a larger pressure drop across the heat exchanger and water will have better thermal contact with the heat exchange tubes. Of course, many of the similarities and differences between the heat exchangers must be considered and a similarity and scaling analysis should be performed before comparing the heat exchanger performance of one to the other.

One concern affecting the accuracy of data taken from the test apparatus for the undergraduate thesis was the potential for water to flow around, rather than through, the tubes since there was a gap with a radial dimension of 0.01 m around the perimeter of the tube bundle. To resolve this issue, the heat exchanger was fitted to a PVC mechanical diverter ("filler

material") with enough flow channels for water to flow through the appropriate ports as shown in Fig. 2.4. The mechanical diverter had a slip fit between the tube and the outer shell of the heat exchanger housing.
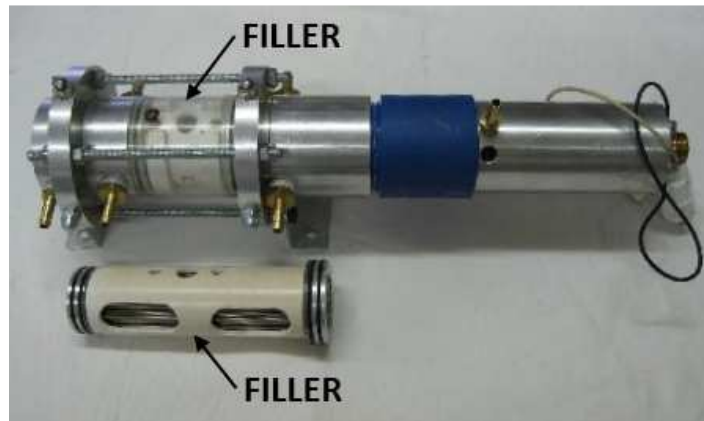
Fig. 2.4. Heat exchanger with tube bundle and filler material

When looking at the tube bank from the perspective of one of the end caps, a simple diagram of the filler material is shown in Fig. 2.5.
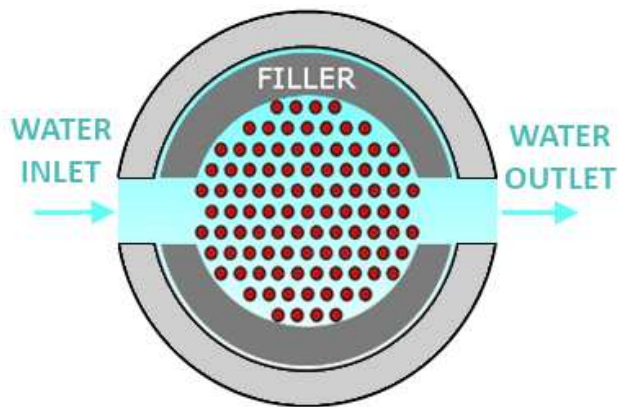
Fig. 2.5. Diagram of filler material adapted to the tube bank

Fig. 2.4 also shows a thermal break made of high density, Air-Pro plastic (shown in dark blue) to minimize conduction heat transfer from the shell of the heater section to the shell around

the tube bundle. With this method, the only appreciable heat that reaches the tube bundle is from the heat that is transferred to the air from the heater element.

2.1.2. DESIGN OF TEST APPARATUS

A Central Pneumatic® (model 93785) single-stage, twin-cylinder compressor pump was adapted for purposes of shuttling air back and forth through the heat exchanger. Part of the customization efforts on this compressor pump involved replacing the gaskets, valve seats, and cylinder by a valve-less, aluminum cylinder head as shown in Fig. 2.6.
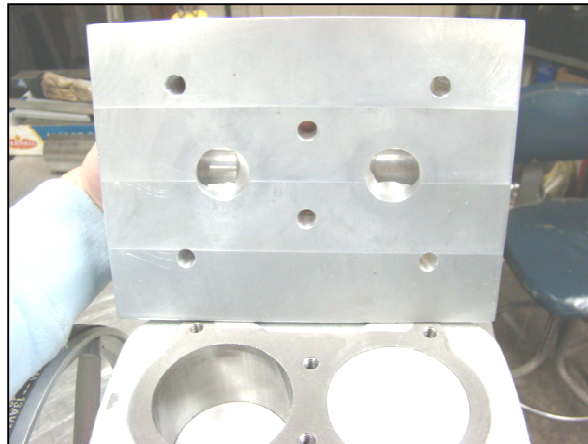
Fig. 2.6. Custom, valve-less compressor pump head

From either side of the custom cylinder head, copper and PVC piping extended to channel air from the compressor pump to the rubber tube isolator devices as shown in Fig. 2.7.

14
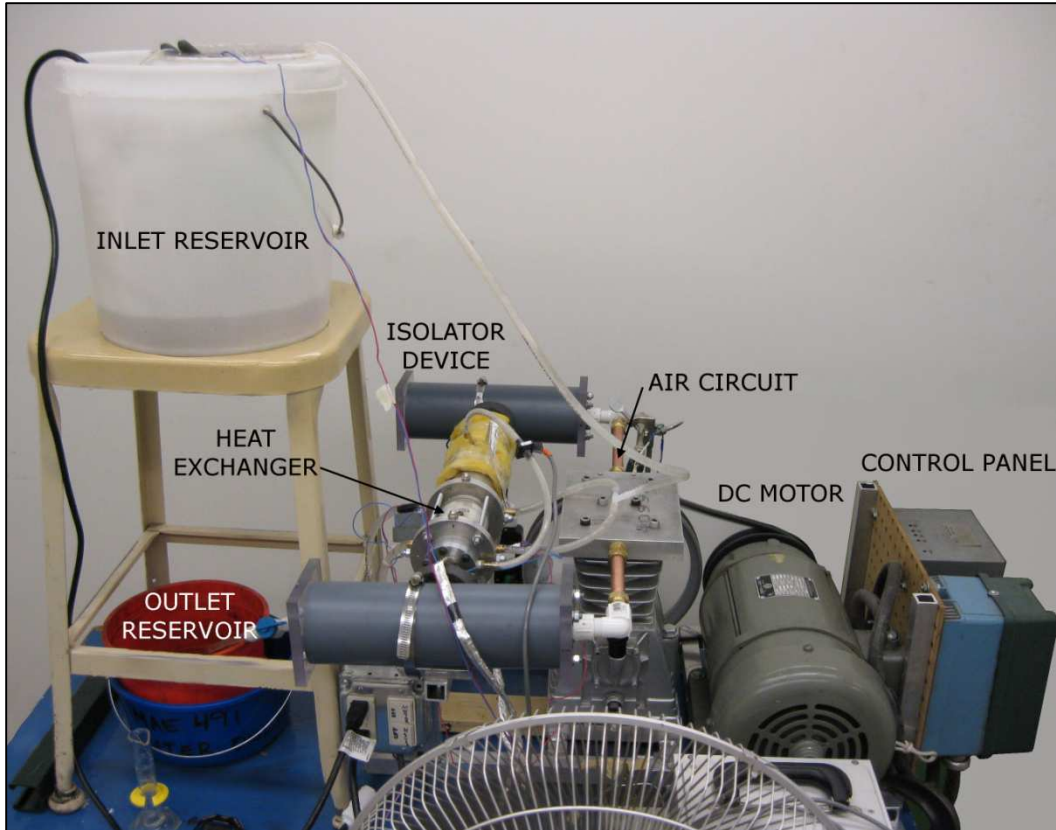
Fig. 2.7. Arrangement of heat exchanger, compressor pump, and connecting channels

The rubber tube isolator devices were necessary in order to isolate unwanted, external heat inputs and minimize airborne oil in the air that oscillated in the tube bundle. The isolator device, as shown in Fig. 2.8, is composed of a section of rubber bicycle tube, machined PVC connectors, clear plastic end caps, NPT brass fittings, miscellaneous fasteners, and an outer PVC shell.
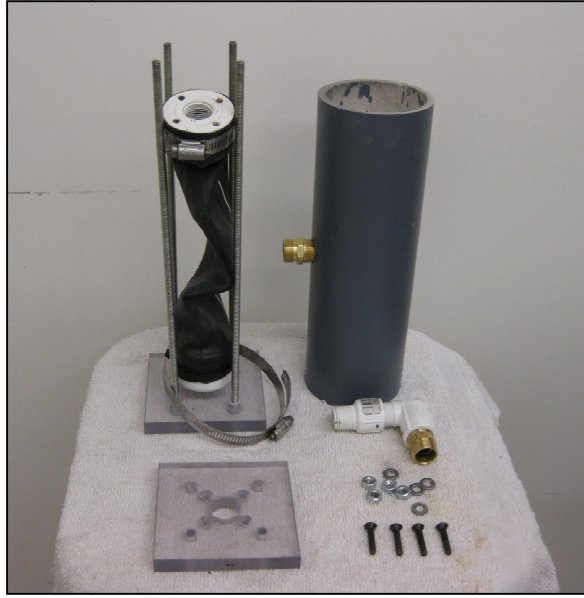
Fig. 2.8. Rubber tube isolator device (disassembled)

The cooler was composed of a tube bundle which sealed against the inner surfaces of a water chamber. O-rings were used to seal the tube bundle against the inner surfaces of the water chamber shell which helped to divide the water chamber from the air plenum chambers at both ends of the tube bundle as shown in Fig. 2.9 (shown without filler material).

Fig. 2.9. Fabricated heat exchanger with separate air and water chambers

The two pistons in the compressor pump are 180° out of phase such that they move a constant volume of air in each cycle without compressing the air. The plenum chambers and the

empty volume in the isolator devices can be thought of as the 'mixing chambers' on either side of the heat exchange tubes. No screens or baffles were used in these chambers.

The fabricated cooler has two inlet and two outlet water ports with an open circuit of water flowing through them in order to maintain a constant inlet water temperature. With such a low flow rate, water conservation and recycling was not an issue. The inlet water was siphoned from an "overflow bucket" with a free surface water level located 0.48 m above the water level in the heat exchanger. The water flow rate was maintained constant via the system in Fig. 2.10.
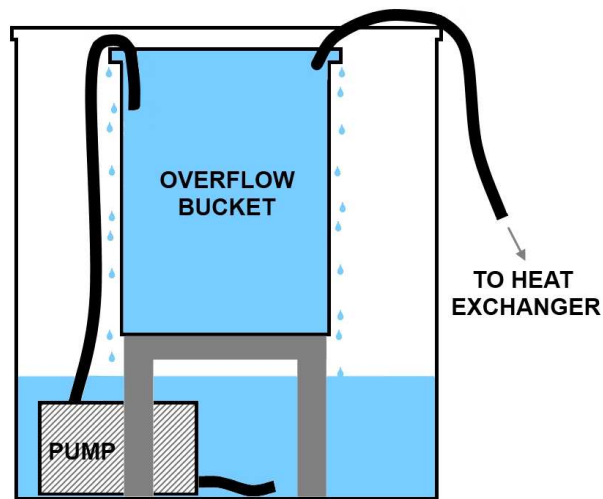
Fig. 2.10. Water siphoning method

In this system, a constant pressure head is maintained due to a smaller, constantly-overflowing bucket which is fed by an aquarium pump located in the larger bucket. The temperature increase of the water due to the aquarium pump was considered negligible and was shown not to vary by more than ± 0.3°C over the course of 4 hours. The water was siphoned through polyvinyl tubing with a 6.35 mm (0.25 in) inner diameter into the heat exchanger. The exit water flow rate was controlled by adjusting a plastic ball valve at the outlet of the heat exchanger as shown in Fig. 2.11.
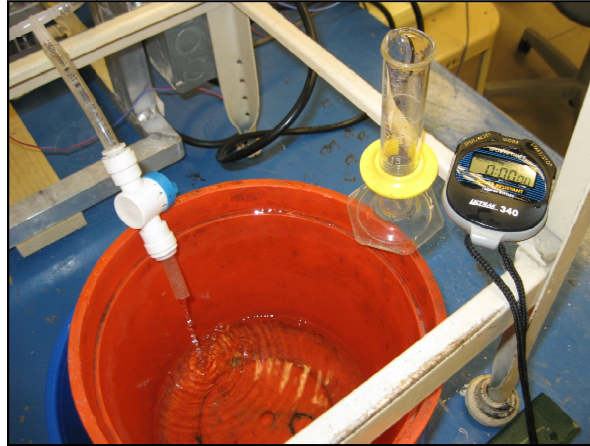
Fig.2.11. Outlet water bucket and water flow rate measuring tools

The outlet water was discharged into another small bucket and was occasionally allowed time to reach room temperature so that it could be reused.

A U.S. Electrical Motors (Model M-15) DC motor was used to power the compressor pump through a v-belt and pulley system. The incorporation of a DC motor facilitated the process of varying the oscillating frequencies since they could easily be controlled using a "manual speed" knob on the control panel as shown in Fig. 2.12.
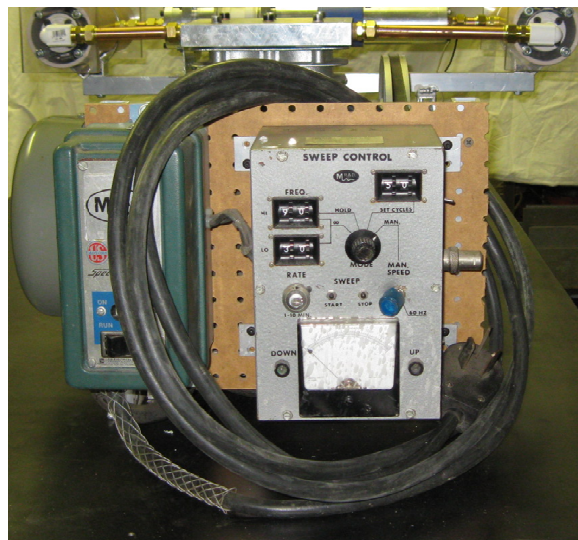
Fig. 2.12. DC motor control panel

The DC motor was able to easily produce any frequency specified between the range of 0.5 to 19.3 Hz (30–1160 RPM). Each revolution of the DC motor incurred a 4:5 reduction through the pulley and resulted in displacing 1.66×10^{-4} m^3 of air in each piston of the compressor pump.

Due to the high level of adaptability of the test apparatus, any component can be switched out with another component and the test rig can be expanded to accommodate additional devices such as a Stirling engine regenerator. This may be useful in future experiments because, in theory, the current test apparatus could be combined with other components that may make it possible to have a functional Stirling engine.

As will be discussed in the following section, one of the main challenges in the design of the test apparatus was the minimization of external heat inputs. This caused many problems with interpreting early batches of data obtained from the test rig due the large margin of error in the results. A drastic redesign of the test apparatus occurred prior to collecting data for the present analysis [18].

2.2. DATA ACQUISITION

The majority of the data in this experiment were collected using LabVIEW and National Instruments (NI) SCXI-1303 and NI SCXI-1321 data acquisition cards and a NI SCXI-1000 chassis. The particular sensors used in this experiment were selected based on their capability to take measurements at high sampling rates, as in the case of air cycling at a maximum of 19.3 Hz. The desired minimum sampling rate for data acquisition was set as 40 Hz, which, despite its appearance, is actually two times larger than the Nyquist frequency since air passes the thermocouples two times during a single revolution of the compressor pump. A 40 Hz minimum sampling rate was also chosen because the author was reaching the limits of physical size of the thermocouples that could sample data at that rate. The thermocouples that were chosen were Omega type J butt-welded thermocouples which had a 0.076 mm (0.003 in) diameter and were capable of sampling at a rate of at least 50 Hz [19]. Water temperatures were measured with Omega special type T spot welded/beaded-type thermocouples with a 0.508 mm (0.020 in) diameter since the water temperatures were not expected to incur temperature fluctuations as rapid

19

as the air temperature fluctuations [19]. The air temperatures used in this analysis were the average temperatures over the course of three cycles of the compressor pump. The average air temperatures were calculated by importing raw temperature data into Engineering Equation Solver (EES) software and using lookup tables to average the data in the columns (see Appendix A for detailed EES code).

A piezoelectric differential pressure transducer was selected to measure the air pressure drop across the tube bundle during the oscillations. The fluctuations in differential air pressure allowed for a method of determining the oscillation frequency using the LabVIEW virtual instrument (VI). A piezoelectric pressure transducer was selected for its relatively low cost and high sampling rates. The pressure sensor was an Omega PX-137-015DV model which measured differential pressures up to 103.4 kPa (15 psi) and had a linearity and hysteresis error of 0.1% full scale (FS) typical or 0.5% maximum [20]. A schematic of the test setup and the location of all data collection points is shown in Fig. 2.13.
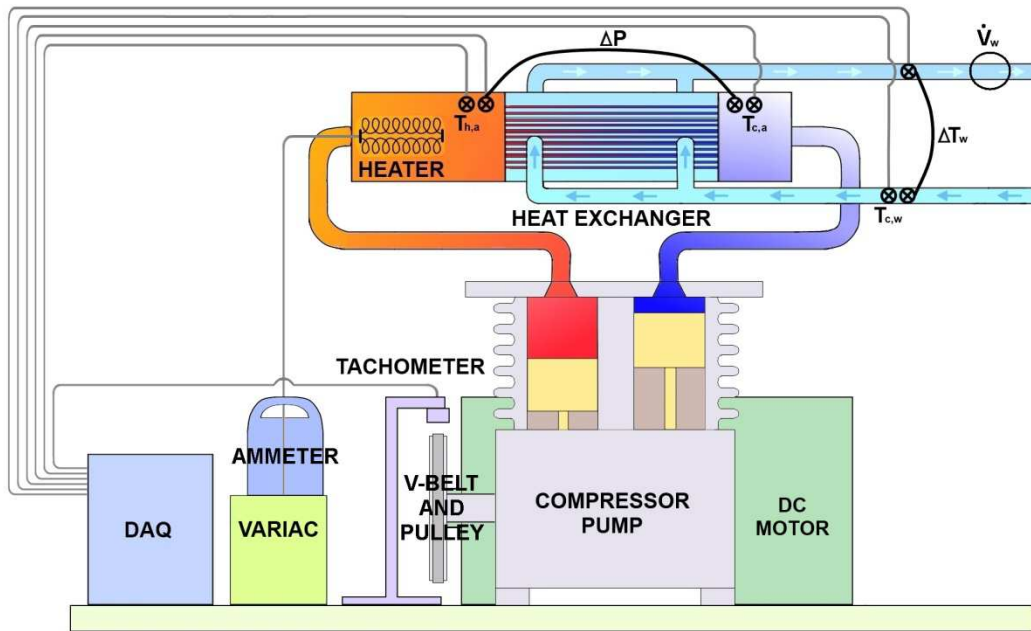

Fig. 2.13. Schematic of test setup and all data collection points

Over the course of all of the experiments, the range of temperatures and pressures recorded by these sensors is shown in Table 2.3 along with other mass flow rate, heater power, and frequency data.

Table 2.3. Range of tested conditions over all experiments

	Minimum	Maximum
$T_{h,a}$ (°C)	122.2	201.8
$T_{c,a}$ (°C)	35.8	48.0
$\Delta P_{a.av}$ (kPa)	$\approx 0\ kPa$	
$\dot{m}_{a,av}$ (kg/s)	2.1×10^{-3}	7.1×10^{-3}
$T_{w,c}$ (°C)	24.2	26.4
ΔT_w (°C)	7.3	14.7
$\dot{m}_w$ (m^3/s)	$\approx 2.26 \times 10^{-3}$	
$\dot{W}_s$ (W)	133.6	201.6
f (Hz)	6.0	19.3

The most notable values in Table 2.3 are the relatively high air temperatures reaching as high as 201.8°C. This temperature was significant because it was found that the high density, Air-Pro plastic that was used in the thermal break between the heater section and the tube bundle section had a melting point of 180 ± 10°C. The extreme temperatures melted the thermal break, which needed to be re-machined and replaced three times during the course of the present experiments. Nevertheless, useful data were collected before the thermal break became weakened to the point where air escaped the system. This issue resulted in the decision to limit the maximum heat input rate to 201.6 W and the minimum oscillation frequency to 6 Hz. Due to the melting incidents, experiments performed at 201.6 W could not be repeated like the other data sets were. As another note, the $\Delta P_{a.av}$ value reported in Table 2.3 is approximately zero since the compressor pump cycled about ambient pressure and an elevated mean cycle pressure was not used in this experiment. Finally, the average mass flow rate of air, $\dot{m}_{a,av}$, was found by a rough calculation involving the oscillation frequency of the compressor pump, the frontal free-flow area inside the tube bank, and volume displaced by each cylinder in the compressor pump. The definition of $\dot{m}_{a,av}$ will be described later in this paper, as well as an explanation of why more accurate

21

methods of obtaining this value could not be implemented. Also, the tachometer shown in Fig. 2.13 was an optical tachometer which would indicate a step function increase in voltage whenever the compressor pump piston closest to the heater was at top dead center (TDC). The data collected from the tachometer was not used in the present analysis; however, the tachometer serves to indicate the phase lag between the compressor pump cycle and the temperatures in the heat exchanger.

Despite exploring more advanced and more accurate methods of measuring water flow rate, the method that was chosen involved a 25 mL graduated cylinder and a stopwatch. At multiple times during each test, the author measured the time to fill the graduated cylinder to the 25 mL mark and converted this value to a volumetric flow rate. This method demonstrated that the water flow rate deviated by only $\pm\ 0.27$ mL s^{-1}.

Finally, the heat rate introduced in the heat exchanger needed to be precisely controlled and measured. The voltage on the heater element was controlled using a VARIAC and the current was monitored with a clip-on ammeter as shown in Fig. 2.14.
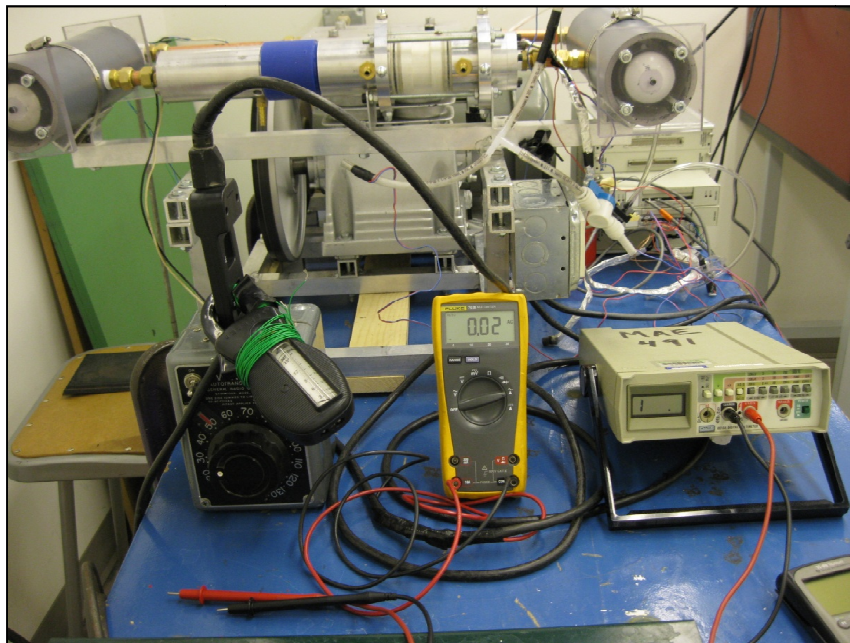
Fig. 2.14. Measurement tools for the calculation of power input to the heat exchanger

A test of linearity was performed on the VARIAC and ammeter and the bias errors of these devices were checked against more accurate multimeters. The bias and precision errors were taken into account before reporting an overall power input value in the present experiment.

Many different methods were used to acquire experimental data on the maximum air velocity, but to no avail. The first of these methods was the use of a Pitot tube which was positioned over one end of one of the tubes in the tube bundle with the heater section removed for ease of access as shown in Fig. 2.15.
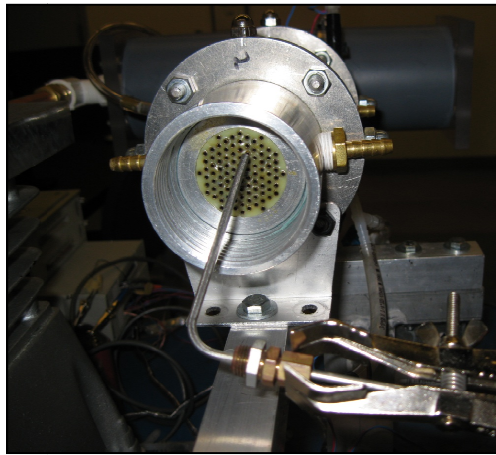
Fig. 2.15. Pitot tube positioned over one end of a tube in the tube bundle

From Fig. 2.15 it is obvious that the Pitot tube was not used in the way that it is intended by the manufacturer [21]. Specifically, there are static pressure taps located circumferentially around the end of the Pitot tube which were not in the air stream since the Pitot tube was too large to insert in the inner diameter of one of the tubes in the tube bundle. There are simply no Pitot tubes known to the author that are small enough to measure the maximum velocity within one of the tubes in the tube bundle.

In another attempt, the Pitot tube was inserted through one of the thermocouple ports and positioned in the center of the air stream in the heater section of the test apparatus as shown in Fig. 2.16. The Pitot tube was held firmly in place with a rubber stopper to prevent air from escaping around the Pitot tube in the thermocouple access port.
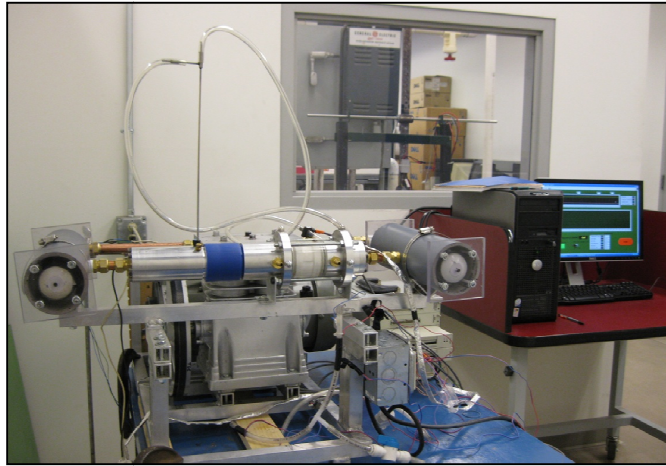
Fig. 2.16. Pitot tube measuring max velocity in the heater section

Data were only acquired with the open end of the Pitot tube facing away from the tube bundle. However, either way that the Pitot tube was oriented would have still violated the minimum unobstructed and unconstricted flow path upstream of the Pitot tube which was specified by the manufacturer as 8.5 diameters of the air duct [21]. The data from both of the Pitot tube tests indicated maximum velocities that were more than 5 times the values that would be considered reasonable. In addition, since the Pitot tube clearly was not positioned in a fully-developed flow region, the measured values are expected to indicate velocities that are lower than the mean velocity; however, the velocities already exceeded reasonable expectations without considering this fact.

The second method used to gain some measure of the maximum air velocity was the use of a lightweight piston that was intended to give a direct measurement of the maximum air stroke length. This required that the air was modeled as plug flow against the face on the piston. The piston was made from nylon and was hollowed-out using a lathe to produce the most lightweight

piston within the author's capabilities. The piston outer diameter was machined to the precision where the piston could pull a moderate vacuum as it slid down the DOM aluminum pipe under due to the pull of its own weight. DOM aluminum tube was used in order to avoid a weld joint common to standard steel tubing that would have caused unwanted friction and impeded the free gliding motion of the piston. The piston was connected to an aluminum rod which extended out of the aluminum tube so that the author could gage the piston's movement against a scale as shown in Fig. 2.17. The orange flag on the end of the piston rod aided the author in taking accurate measurements of the stroke length.
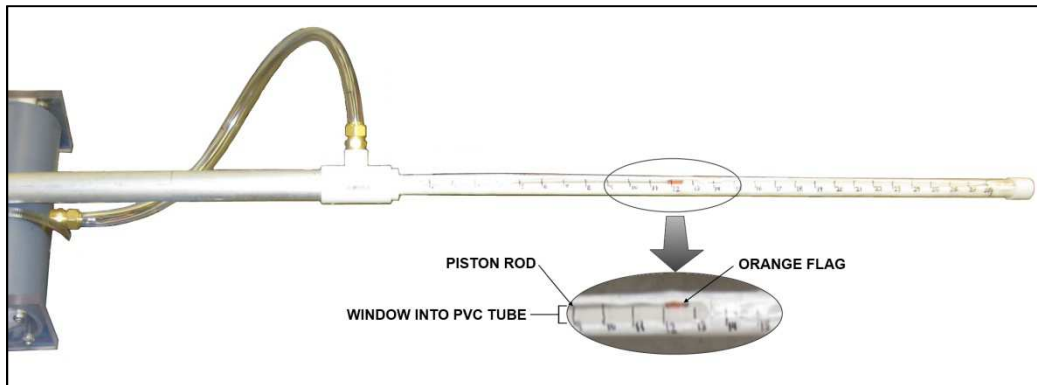
Fig. 2.17. Scale used to measure stroke length in the piston/tube experiments

The piston/tube device was first connected directly to the outlet of the compressor pump. During this experiment, with every few oscillations, the piston was observed to wander to the far end of the scale although it had started in a position where it was oscillating around the midpoint. Therefore, a second test was run with the piston/tube device located between the rubber tube isolator device so that it had both a pressure and vacuum applied simultaneously to either side of the piston as shown in Fig. 2.18.
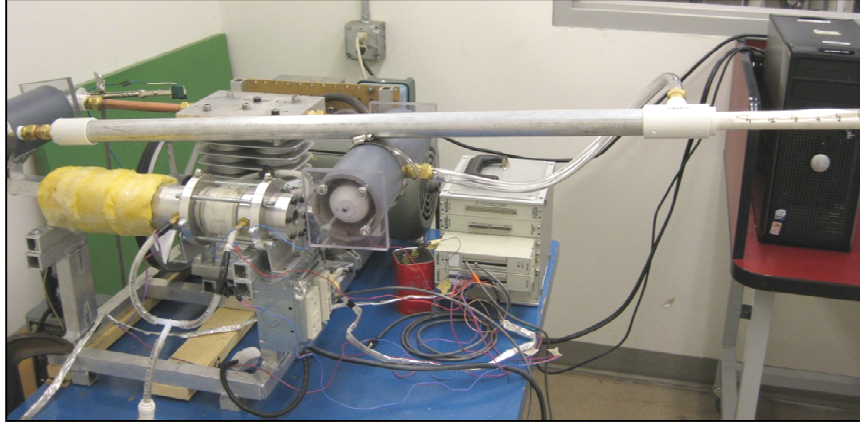
Fig. 2.18. Piston/tube device located between the isolator devices

Fortunately, the piston did not wander nearly as much, but the resulting data was not quite what was expected. Similar to the Pitot tube tests, the stroke lengths corresponded to a calculated amount of air displacement (when multiplied by the frontal area of the piston head) that was far too large to be reasonable. In fact, as shown in Fig. 2.19, at only 1.67 Hz (100 RPM), the stroke length was large enough to indicate that 2.79×10^{-4} m^3 of air was being displaced (according to the data including backpressure), although the capacity of each of the compressor pump cylinders was only 1.66×10^{-4} m^3.
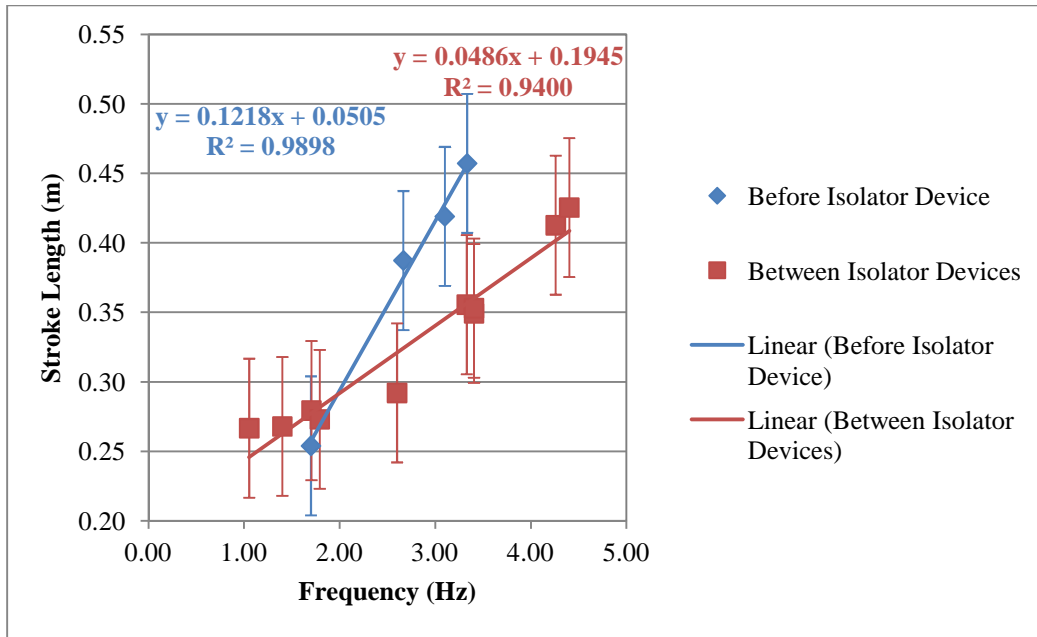
Fig. 2.19. Piston/tube experimental data on stroke length

The unreasonably large volumes calculated from this experiment are easily attributed to error due to the inertia of the piston which would tend to indicate longer stroke lengths than actually realized. Unfortunately, there were no other methods known by the author to account for this effect, and after many attempts to calculate the air velocity directly, the author had to result to theoretical equations rather than experiments. Neglecting compressibility effects and any dampening effects by the rubber tube isolator devices, the maximum stroke length, x_{max}, was finally found by dividing the volume of air displaced by each piston in the compressor pump by the combined frontal area of all the tubes in the tube bank to yield a maximum stroke length (assuming plug flow) of 1.41 m.

2.2.1. ERROR MINIMIZATION

Baseline tests were performed at each oscillatory frequency with the heater element turned off. Any external heat loads that were observed during these tests should be thought of as merely a byproduct of increasing the frequency and contributing additional friction effects. As shown in Fig. 2.20, these external heat load contribution loads were minimal, especially when

27

compared to the external heat loads that were present before the modifications to the test apparatus were made. Every method, within reason, has been employed to minimize these heat inputs. For instance, the heat exchanger is moved further away from the compressor pump heat sink, the air that cycles in the compressor pump is separate from the air in the heat exchanger due to the rubber tube isolator devices, a plastic thermal break is located between the heater section and the air plenum chamber, and a fan is used to blow ambient air over the test apparatus. All of these efforts resulted in dramatic improvements in accuracy of the data. When comparing the maximum temperature rise of the cold side air, the temperature rise was less than 0.5 °C over 420 seconds in the present experiment whereas it was formerly 10 °C over the same amount of time.
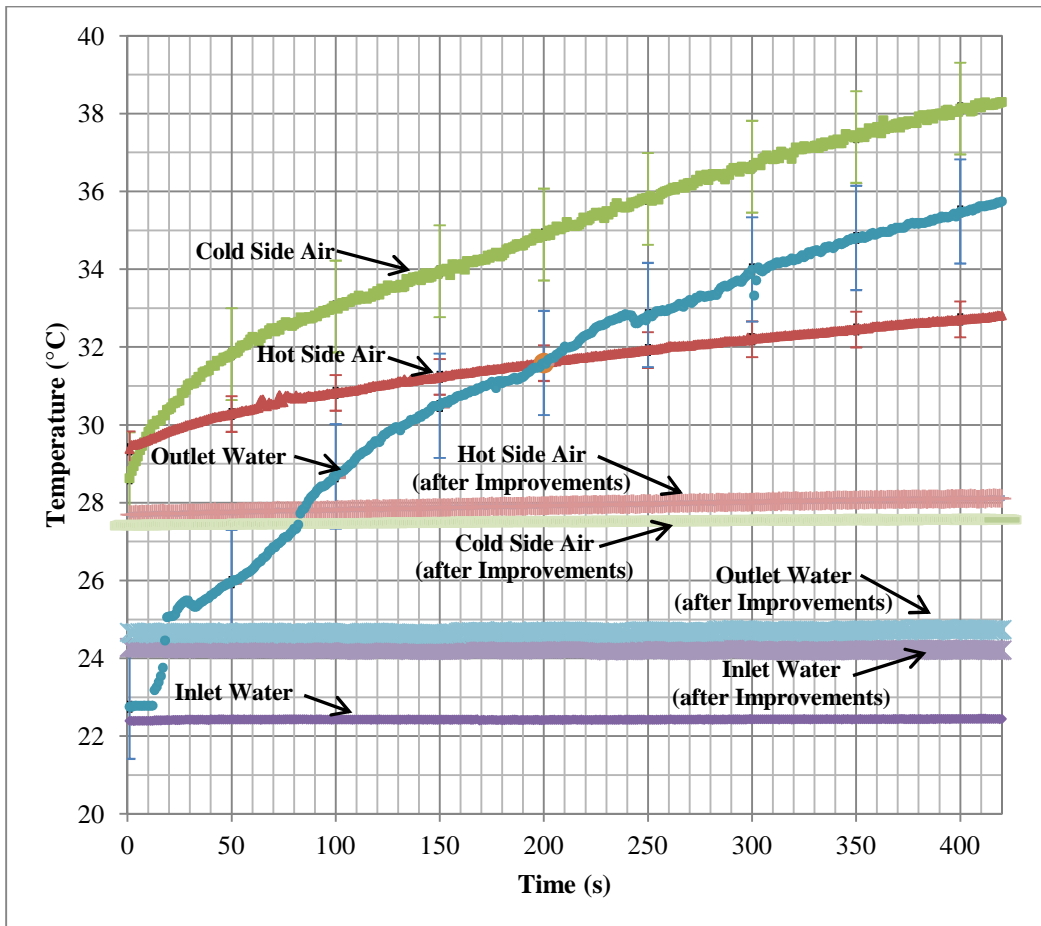
Fig. 2.20. External heat input effects on fluid temperatures during startup

Uncertainty of the thermocouples in Fig. 2.20 was only ± 1.2 °C for the hot and cold side air thermocouples. The thermocouples measuring water had slightly lower uncertainties of ± 0.10 °C and ± 0.13 °C for the hot and cold water thermocouples, respectively.

2.2.2. UNCERTAINTIES IN RESULTS

        When analyzing values from the raw data sampled at 1000 Hz in Fig. 2.21, it can be seen that the cold air temperature (and likewise, the hot air temperature, although not shown) has a logical correlation with the pressure drop across the tube bundle and the position of the pistons in the compressor pump. To clarify, tachometer voltage does not correlate with either of the scales on the y-axes of Fig. 2.21 since it simply serves the purpose of indicating when the piston in one of the compressor pump cylinders reaches its top dead center (TDC) position, and thus, air movement ceases momentarily. The tachometer data indicate a step function increase when the reflective sticker passes by the optical sensor with each rotation of the pulley.
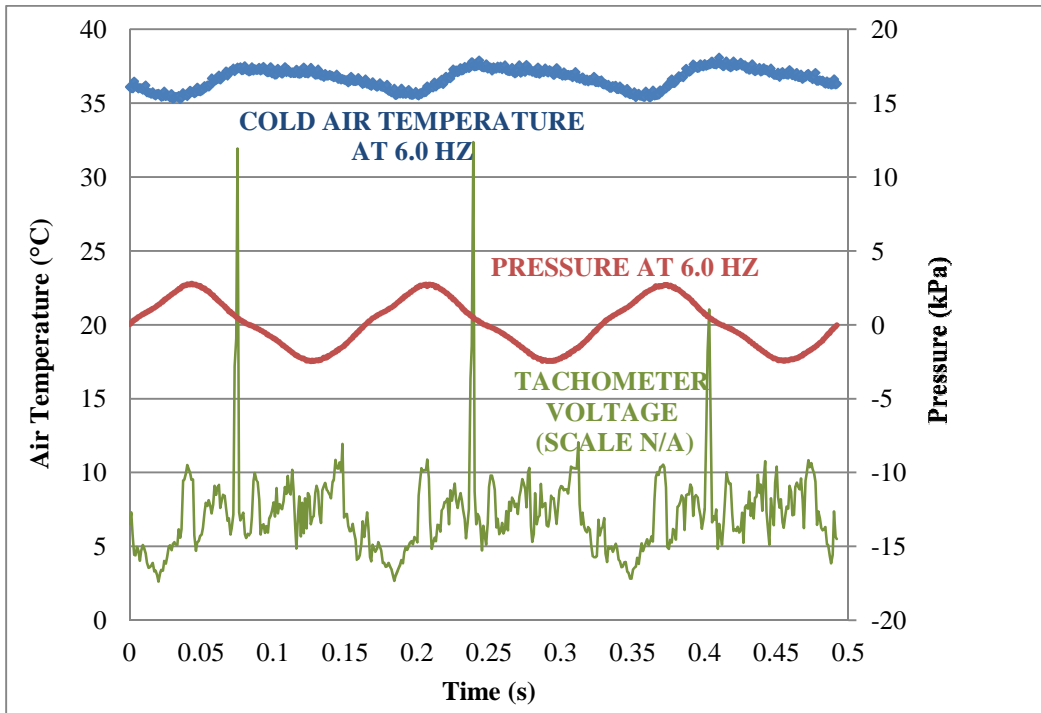
Fig. 2.21. Three cycles of raw temperature and pressure data at 6 Hz

29

In Fig. 2.21, the cold air temperature curve does not follow a perfect sinusoidal shape, however, this can easily be explained by the location of the thermocouple relative to the air stream since the thermocouple junction is somewhat shielded in a pocket on the cold-side end cap of the heat exchanger. The cold air thermocouple receives a blast of cold air as air leaves the tube bundle, but is insulated from the stronger blast of air upon its return from the compressor pump cylinder. The maximum and minimum values on the cold air temperature curve follow the peaks on the pressure and tachometer curves, as expected. Thermocouple error was too small to be shown in Fig. 2.21 with error bars since it was only ± 1.2 °C for the hot and cold air thermocouples. Pressure sensor error was also too small to be shown on Fig. 2.21 since it was only ± 0.5% maximum.

As noted previously, the piezoelectric pressure transducer was only used to determine the oscillation frequency rather than used for pressure data. This was due to the pressure drop data being outside of the display range as it exceeded ± 3.5 kPa as indicated in Fig. 2.22.
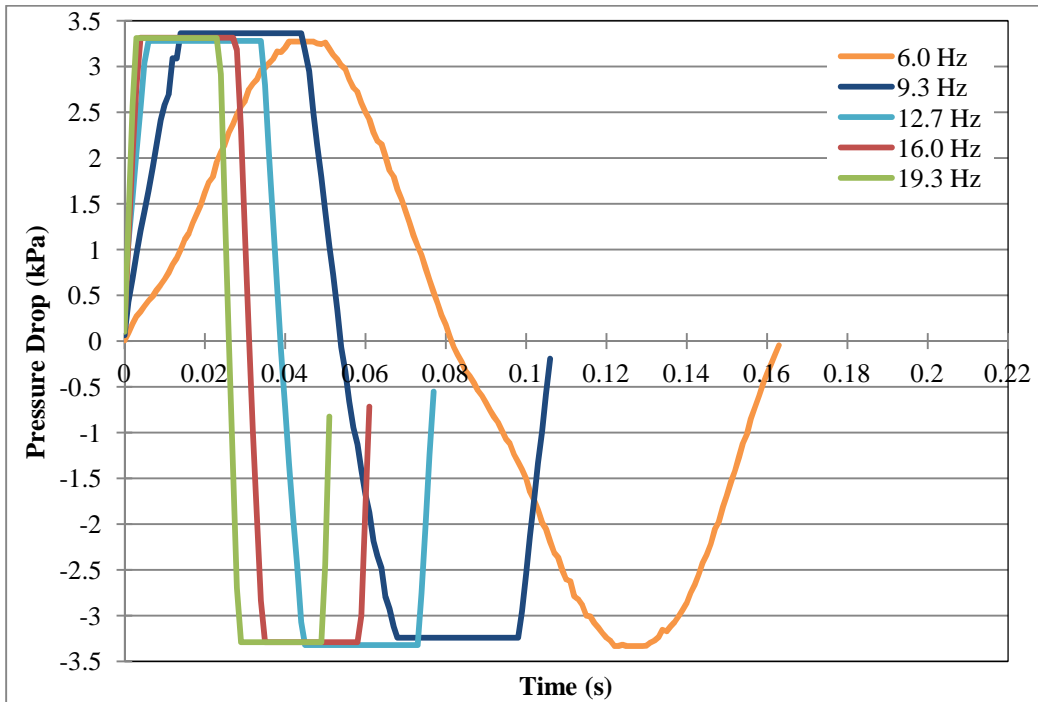
Fig. 2.22. One cycle of pressure drop data

30

While Fig. 2.22 clearly indicates the time taken for each cycle, it does not provide any information on the relative amplitudes of the pressure drop since the only complete set of pressure drop data is at the lowest frequency when the pressure drop, and thus, the turbulent effects of the air were not as large.

The uncertainties in the results of this research were evaluated using a steady-state method detailed by R. J. Moffat to determine the overall uncertainty [22]. As an example of Moffat's method, the overall uncertainty in the heat transferred to the water, $\dot{Q}$, will be calculated. $\dot{Q}$ is defined as:

$$\dot{Q} = \frac{\dot{V}\, c_p\, \left(T_{h,w} - T_{c,w}\right)}{\rho} \tag{7}$$

where $\dot{V}$ is the volumetric flow rate of water, c_p the isobaric specific heat of water, $T_{h,w}$ the hot water temperature, $T_{c,w}$ the cold water temperature, and ρ the density of water. All temperature data in the present experiment have been shifted up or down according to the calibration error determined from an ice bath test. The remaining precision error is accounted for by using Moffat's formula in (8) [22]. The steady-state relative error in the calculation of $\dot{Q}$ is as follows, where the numerator is the precision error and the denominator is the maximum value of measured variable [22]:

$$\frac{\delta \dot{Q}}{\dot{Q}} = \left\{ \left(\frac{\delta \dot{V}}{\dot{V}}\right)^2 + \left(\frac{\delta T_{h,w}}{T_{h,w}}\right)^2 + \left(\frac{\delta T_{c,w}}{T_{c,w}}\right)^2 \right\}^{\frac{1}{2}} \tag{8}$$

where δ indicates a finite change in the following variable. In the experiment, $T_{h,w}$ was found by adding the temperature given by the differential thermocouple to the inlet water temperature value, $T_{c,w}$, which is already accounted for in (8). Therefore, the $T_{h,w}$ in (8) will be replaced with the precision error and maximum values recorded by the differential thermocouple measuring the temperature difference between the inlet and outlet water flows. The overall uncertainty in the heat transferred to the water is calculated as follows [22]:

$$\frac{\delta \dot{Q}}{\dot{Q}} = \left\{ \left(\frac{2.7 \times 10^{-7} \frac{\text{m}^3}{\text{s}}}{1.1 \times 10^{-5} \frac{\text{m}^3}{\text{s}}} \right)^2 + \left(\frac{0.10 \, ^\circ\text{C}}{38 \, ^\circ\text{C}} \right)^2 + \left(\frac{0.13 \, ^\circ\text{C}}{27 \, ^\circ\text{C}} \right)^2 \right\}^{\frac{1}{2}} \tag{9}$$

which yields a relative error of up to $\pm 5.0 \, W$, or 2.5% of $\dot{Q}$ when $\dot{Q}$ is at the maximum tested heat

rate of 202 W. Note that the error in fluid properties that were referenced in the Engineering

Equation Solver are considered to be negligible with respect to the variations in the measured data

and do not appear in (8) and (9). For a sample of the Engineering Equation Solver code used in

this analysis, refer to Appendix A.

2.3. PROCEDURE FOR ANALYSIS

Two types of analyses are performed on the data: a dimensional and nondimensional

approach. In the dimensional approach, correlations for the overall heat transfer coefficients are

reported; however, heat transfer data from oscillating flow experiments are more useful for

comparison to other data when in terms of nondimensional parameters. When data are presented

in nondimensional form, a scaling and similarity procedure will still need to occur before the data

from the present experiment can be applied to other heat exchangers.

2.3.1. DIMENSIONAL APPROACH

The approach for determining the heat transfer coefficients was divided into three steps

by necessity since there is no fully-encompassing algorithm for this process. The overall heat

transfer coefficient was determined first, followed by the outside heat transfer coefficient, so that

the inside heat transfer coefficient could be isolated in (10) provided that all other symbols are

known. The overall heat transfer coefficient, U, is defined as:

$$U = 1 / \left(\frac{1}{h_o} + \frac{l}{k_W} + \frac{1}{h_i} \right) \tag{10}$$

where h_o is the heat transfer coefficient at the steel and water interface, l the tube wall thickness,

k_{ss} the stainless steel tube wall conductivity, and h_i the heat transfer coefficient at the steel and air

interface.

The analytical method used to solve for the overall heat transfer coefficient involved Newton's law of cooling to solve for the overall heat transfer coefficient, U:

$$\dot{Q} = U\, A_{av}\, \Delta T_{lm} \tag{11}$$

where $\dot{Q}$ is the total heat rate transferred through the tube walls to the water, A_{avg} the average heat transfer area of the tube bank, and ΔT_{lm} the log mean temperature difference defined as [23]:

$$\Delta T_{lm} = \frac{\Delta T_1 - \Delta T_2}{\ln(\Delta T_1/\Delta T_2)} \tag{12}$$

where for counterflow ΔT_1 and ΔT_2 are defined by [23]:

$$\Delta T_1 = T_{h,a} - T_{h,w} \tag{13}$$

$$\Delta T_2 = T_{c,a} - T_{c,w} \tag{14}$$

where the subscripts h and c denote the hot and cold fluid temperatures, respectively. This approach was based on the assumption of constant surface temperature along the length of the tubes. The heat rate value in (11) was determined to be the heat rate gain by the water, $\dot{Q}_w$, since this is the value that represents the heat that is transferred through all of the thermal barriers shown in Fig. 1.3.

Research by W. A. Khan *et al.* provided a helpful coefficient to modify the standard Nusselt number equation shown in (15) in order to find the outside heat transfer coefficient [24]:

$$Nu_o = \frac{h_o\, d_o}{k_w} = C\, Re^{1/2}\, Pr^{1/3} \tag{15}$$

where Nu_o is the Nusselt number for the outside of the tube bank, h_o the outside heat transfer coefficient, d_o the outside diameter of the tubes in the tube bank, k_w the thermal conductivity of the water, Re the Reynolds number of the water which is defined in (2), Pr the Prandlt number of the water, and C a coefficient determined experimentally by Khan *et al.* for staggered tube banks [24]:

$$C = \frac{0.61\, S_t^{0.091} S_l^{0.053}}{[1 - 2\exp(-1.09\, S_l)]} \tag{16}$$

33

where S_t is the transverse distance between tubes in the tube bank and S_l the longitudinal distance between tubes in the tube bank. Khan *et al.* assures that (16) is valid for a dimensionless longitudinal pitch within the bounds of $1.05 \leq X_l \leq 3$, and a dimensionless transverse pitch within the bounds of $1.05 \leq X_t \leq 3$ [24]. For the present experiment, X_l is within these bounds at a value of 2.74; however, X_t slightly exceeds these bounds at a value of 3.16 [24]. Due to the minor differences in these tested parameters, Khan *et al.*'s coefficient will still be considered valid for the present experiment. The last value that remains unsolved from (10) is the inside heat transfer coefficient, h_i, however, all other symbols in this equation have known values, so (10) is simply rearranged to solve for h_i.

2.3.2. NONDIMENSIONAL APPROACH

The development of a Nusselt number correlation for the overall heat transfer coefficient in a Stirling engine heat exchanger was out of reach since it would involve too many independent variables and many questions would arise on whether certain geometrical properties of the heat exchanger could adequately represent the heat exchanger as a whole. The most useful form of the outcomes from the present experiment is thought to be the correlation between the Nusselt number for the oscillating air, Nu_i, and various other nondimensional parameters such as Reynolds numbers. There are few Nusselt numbers that are presented for oscillating air flow, whereas there are numerous correlations for the Nusselt number for the unidirectional water flow over tube banks that can be combined with the present results to find the overall heat transfer coefficient [24], [6]. Therefore, only the correlation for the Nusselt number for oscillating air will be presented here and readers are recommended to defer to research performed by Khan *et al.* to find the particular correlation for other modes of heat transfer they may have in their heat exchanger [24].

Most results from research on oscillating flows are reported in nondimensional parameters. Therefore, in an attempt to do the same, the Nusselt number for air will be presented in terms of the nondimensional parameter(s) for which it is shown to be the strongest function. In general, the Nusselt number is defined as:

34

$$Nu = \frac{h_i \, d}{k} \tag{17}$$

where, in the case of air, h_i is the inside heat transfer coefficient, d the inner tube diameter, and k the thermal conductivity of air. The Nusselt number in oscillating flow is generally a function of the standard Reynolds number and the kinetic Reynolds number, where the kinetic number is defined in (3) and should only include air properties and the diameter of the inside of the tubes. The standard Reynolds number is defined in a unique way for oscillating flow by F. de Monte *et al.* by [6]:

$$Re = \frac{\dot{m} \, d_{hyd}}{A_f \, \mu} \tag{18}$$

where A_f is the frontal, free-flow area inside the tube bundle, μ the dynamic viscosity of air, d_h the hydraulic diameter defined by [6]:

$$d_{hyd} = \frac{4 \, A_f \, L}{A_i} \tag{19}$$

and $\dot{m}$ is the average mass flow rate of air which is approximated by:

$$\dot{m} = \rho \, u \, A_f \tag{20}$$

where ρ is the density of air and u the velocity of air. Due to the previously mentioned complications with obtaining direct measurements of the time-varying mass flow rate and velocity of air (as detailed in Chapter 2.2), the velocity of air was defined simply by:

$$u = \frac{2 \, f \, V}{A_f} \tag{21}$$

where f is the oscillatory frequency and V the volume of air displaced by the piston in the compressor pump.

2.3.3. PROCEDURE FOR COMPARISON TO OTHER METHODS

Only the values for inside heat transfer coefficients will be compared to other research since no other results or correlations have been presented in other research for heat exchangers that resemble the heat exchanger in the present experiment. The method that will be used for

35

comparison is based on a correlation determined experimentally by Zhao and Cheng [10]. In their

experiment, they developed a correlation for a space-time averaged Nusselt number for laminar,

oscillating flow which is intended to emphasize the greater role played by the kinetic Reynolds

number with respect to the dimensionless oscillation amplitude in their Nusselt number formulas

[10]. Zhao and Cheng defined the space-cycle averaged Nusselt number as [10]:

$$Nu = \frac{\dot{q}_W \, d_i}{k(T_W - T_m)} \tag{22}$$

where T_W is the tube wall temperature, T_m the mean temperature of the working fluid, and $\dot{q}_W$ the

rate of heat flux through the wall. In the present research, however, (22) could not be used

because the tube wall temperatures were not able to be measured. To compare Zhao and Cheng's

correlation to the present results, the present data will be arranged in a form similar to Zhao and

Cheng's equation for the Nusselt number of air which is scaled down by the dimensionless

oscillation amplitude raised to the power of 0.85 [10]:

$$Nu/A_\omega^{0.85} = 0.02 \, Re_\omega^{0.583} \tag{23}$$

where Re_ω is the kinetic Reynolds number defined previously in (3) and A_ω the dimensionless

oscillation amplitude defined in (5) [10].

Chapter 3: RESULTS

All data presented in this section were obtained under steady-state conditions. Steady state was defined as the point when the most variable temperature—the hot air temperature— did not change by more than ± 1.0 °C over a time period of 4 minutes as viewed on the LabVIEW virtual instrument display within the limits of the display rate of 1 Hz. The display rate of 1 Hz should not be mistaken for the data sampling rate which was 1000 Hz. Steady state was typically reached within 45 minutes after a cold start, but steady state was usually reached within 20 minutes for every test thereafter.

3.1. TEMPERATURES

On the basis of temperatures, the gap between the hot and cold side air temperatures is shown to close at an exponentially increasing rate as the oscillation frequency increases from 6.0 to 19.3 Hz, as shown in Fig. 3.1.
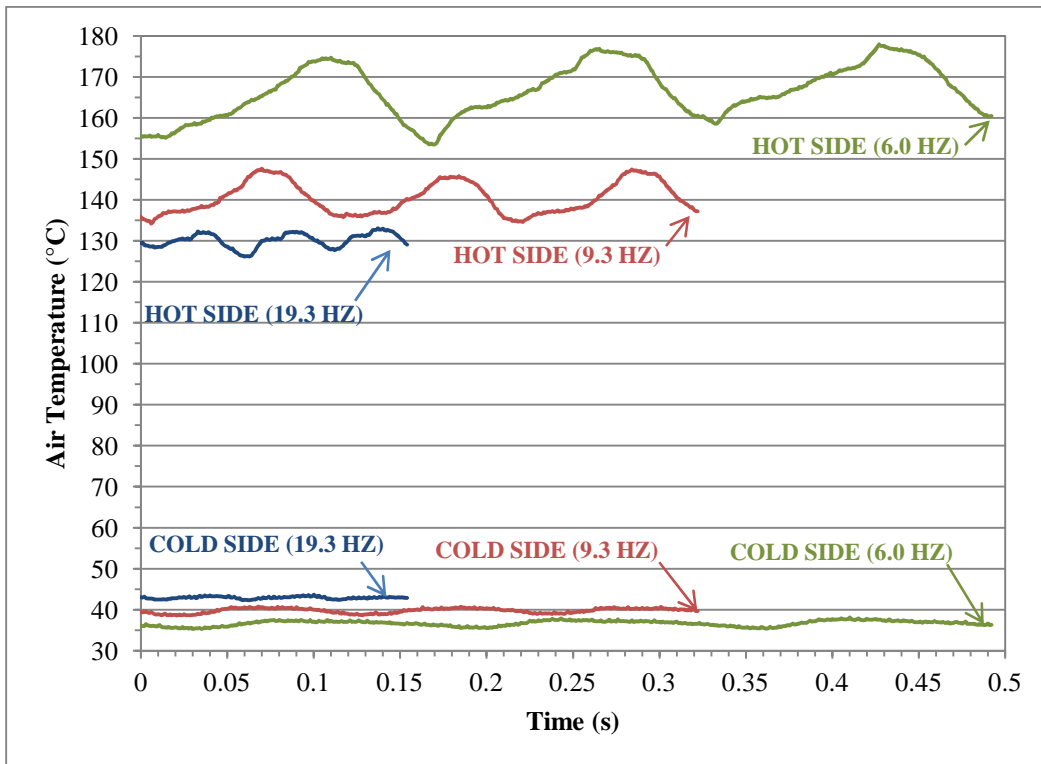

Fig. 3.1. Three cycles of raw data for air temperatures at various oscillation frequencies

Once again, error bars are not shown on Fig. 3.1 due to the extremely low uncertainties of ± 1.2 ℃ for the hot and cold side air thermocouples. Another feature of Fig. 3.1 is the definition of cooling and heating half-cycles as the air is pulsed back and forth over the hot and cold side thermocouples. Three distinct cycles are visible in Fig. 3.1.

3.2. HEAT TRANSFER COEFFICIENTS

The featured result from the present research is the overall heat transfer coefficient as a function of oscillation frequency. While the frequency increases from 6.0 to 19.3 Hz in Fig. 3.2, the overall heat transfer coefficient increases accordingly with a power law fit from 21.5 to 46.1 $W\,m^{-2}\,K^{-1}$.
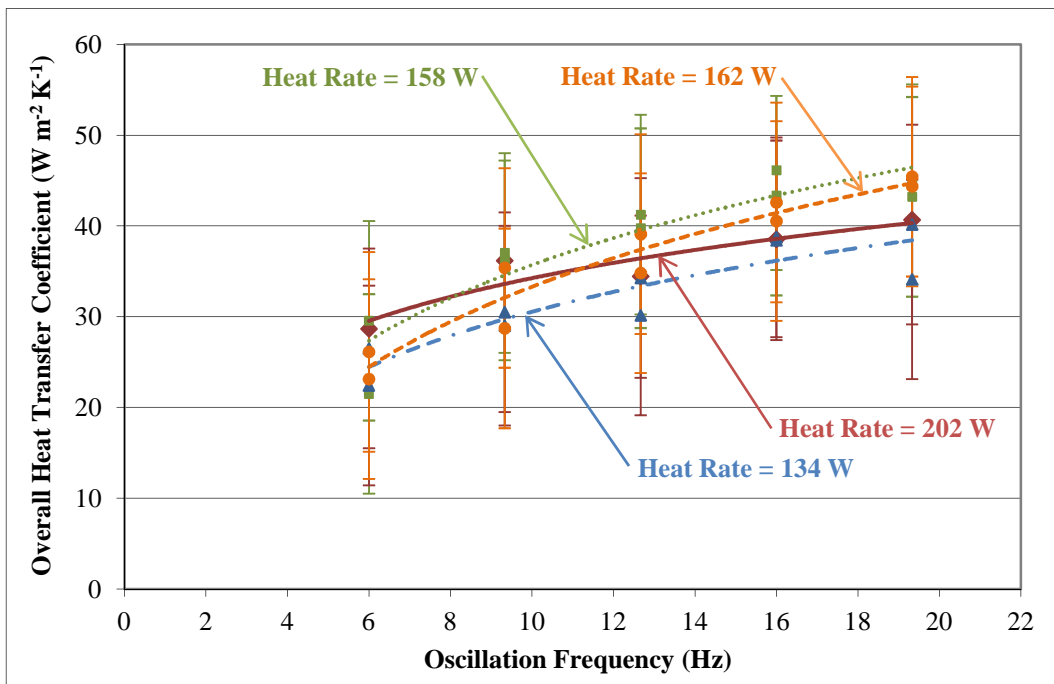

Fig. 3.2. Overall heat transfer coefficients as a function of oscillation frequency

Fig. 3.2 also indicates that the overall heat transfer coefficient is independent of the input heat rate, as it should. In general, heat transfer coefficients must be able to be presented independent of heat

rate and surface area for heat transfer. The higher overall heat transfer coefficient at high

oscillation rates is most likely the cause of the hot and cold air temperatures approaching each

other in Fig. 3.1. The relatively low water flow rate of 0.002 kg s^{-1} (which is held constant in

Fig. 3.2) tends to increase the overall heat transfer coefficient values by allowing the water more

time to pick up additional heat to carry away from the system. A low water flow rate is also

important to this research because air is less efficient at transferring heat, and by slowing down the

rate of water flow, the air is able to transfer a larger amount of heat to a given mass of water

flowing through the heat exchanger.

Table 3.1 shows that the overall heat transfer coefficients increase as a function of

increasing oscillation frequency—mainly due to the inside heat transfer coefficient. In fact, the

outside heat transfer coefficient should be independent of oscillation frequency (since the outside

of heat exchange tubes are not in contact with an oscillating fluid). The variation in h_o values in

Table 3.1 is attributed to the variation in water temperatures at different frequencies which has a

small effect on fluid properties of the water. The minimum and maximum value of the heat

transfer coefficients across all heat rates are shown in Table 3.1.

Table 3.1. Heat transfer coefficients at various oscillation frequencies

	U (W m^{-2} K^{-1})	h_i (W m^{-2} K^{-1})	h_o (W m^{-2} K^{-1})
$f = 6.0$ Hz	24.5–28.7	25.7–30.4	
$f = 9.3$ Hz	29.8–36.6	31.7–39.5	
$f = 12.7$ Hz	32.2–40.5	34.5–44.1	768–787
$f = 16.0$ Hz	38.5–44.7	41.7–49.2	
$f = 19.3$ Hz	37.1–44.9	40.1–49.3	

The value of the overall heat transfer coefficient and inside heat transfer coefficient are nearly the same, but the inside heat transfer coefficient increases slightly more with increasing oscillation frequencies. The outside heat transfer coefficient is much larger than the others due to the greater efficiency of heat transfer at the water and tube wall interface when compared to the air and tube wall interface.

From the data in Table 3.1, it might appear that the inside heat transfer coefficient has reached a point of saturation or perhaps an optimum frequency for heat transfer since the inside heat transfer coefficient ranged from 41.7 to 49.2 at 16.0 Hz and from 40.1 to 49.3 at 19.3 Hz. Thus, the average inside heat transfer coefficient was higher at 16.0 Hz than at 19.3 Hz. However, upon further inspection of this effect in Fig. 3.3, the slight differences in the inside heat transfer coefficient values become less significant when considering the $\pm$ 11% bounds of error on the inside heat transfer coefficient value.
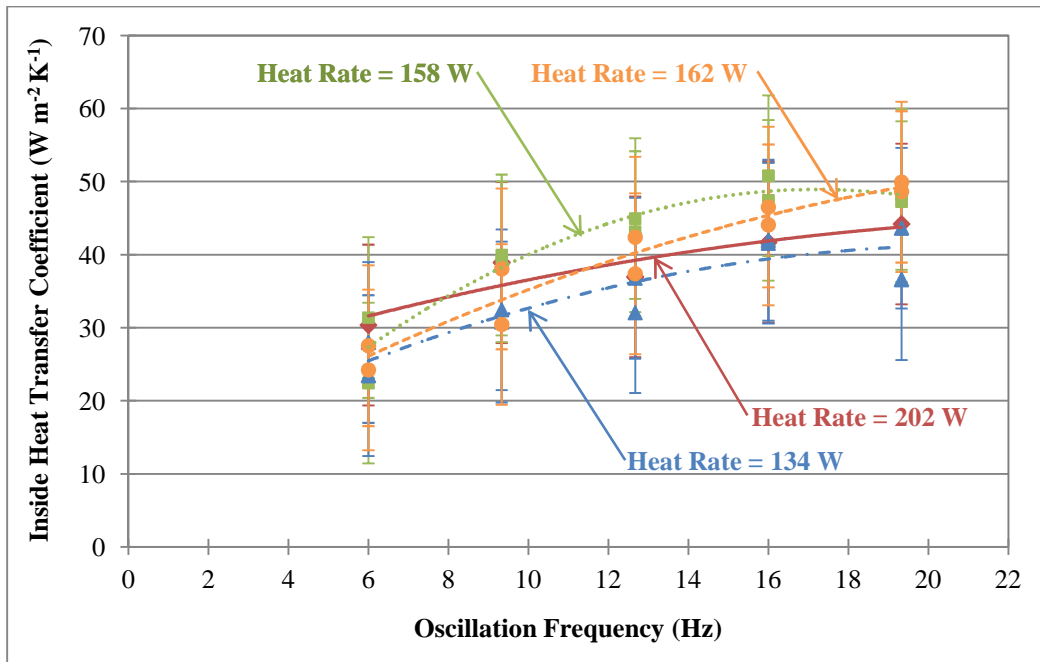

Fig. 3.3. Inside heat transfer coefficients as a function of oscillation frequency

Furthermore, most of the curves in Fig. 3.3 indicate that the inside heat transfer coefficients are slowly approaching a plateau and that neither a saturation point nor optimized frequency has been reached in this range with enough certainty to be conclusive.

As another check on the data, the heat transfer coefficients are presented in terms of their inverses, or thermal resistances. The overall resistance of the heat exchanger is defined as:

$$R_{overall} = R_{i,conv} + R_{cond} + R_{o,conv} \tag{24}$$

and can be calculated using:

$$R_{overall} = \frac{1}{U \, A_{av}} \tag{25}$$

$$R_{i,conv} = \frac{1}{h_i \, A_{av}} \tag{26}$$

$$R_{cond} = \frac{l}{k_W \, A_{av}} \tag{27}$$

$$R_{o,conv} = \frac{1}{h_o \, A_{av}} \tag{28}$$

where $R_{overall}$ is the overall thermal resistance, $R_{i,conv}$ the convection resistance on the inside of the tubes, R_{cond} the conduction resistance through the tubes, $R_{o,conv}$ the convection resistance on the outside of the tubes, U the overall heat transfer coefficient, h_i the inside heat transfer coefficient, h_o the outside heat transfer coefficient, l_w the tube wall thickness, k_{ss} the thermal conductivity of the tube wall, and A_{avg} the average heat transfer area. Using (24)–(28), the thermal resistance values are shown in Table 3.2 using average values of the heat transfer coefficients.

Table 3.2. Thermal resistance values

$R_{overall}$ (K W^{-1})	0.42
$R_{i,conv}$ (K W^{-1})	0.39
R_{cond} (K W^{-1})	4.3×10^{-4}
$R_{o,conv}$ (K W^{-1})	1.9×10^{-2}

Table 3.2 shows that the largest contributor to the overall thermal resistance is the convection thermal resistance on the inside of the tubes. The thermal resistance on the outside of the tubes is only 5% of the total thermal resistance while the thermal resistance by conduction through the tubes is less than 1% of the total thermal resistance. The differences between these thermal resistances are further emphasized in Fig. 3.4.
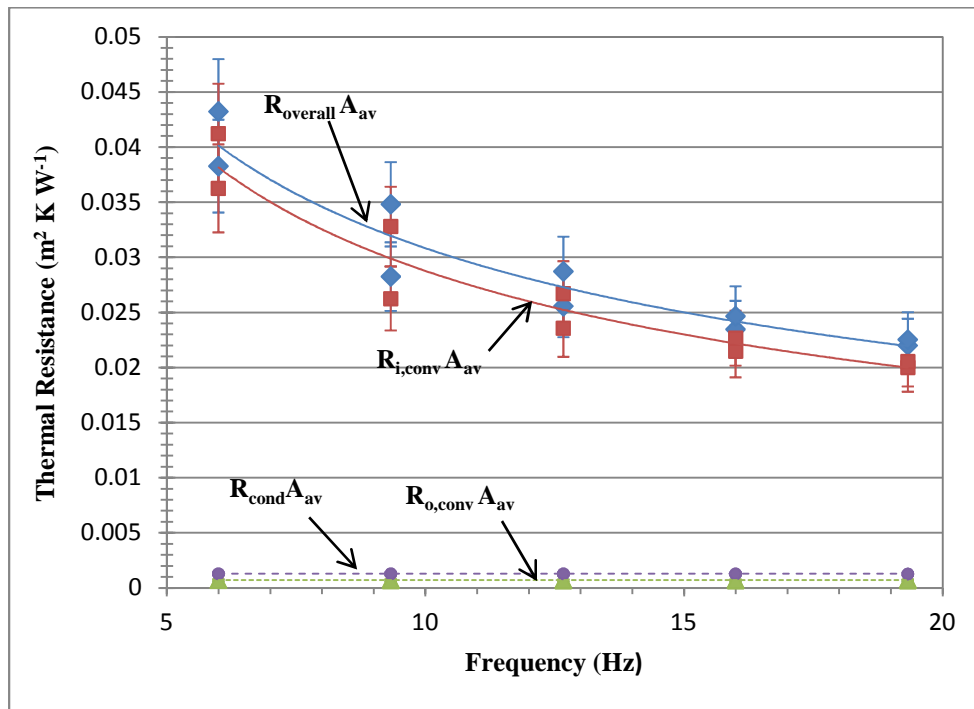

Fig. 3.4. Thermal resistances as a function of frequency

As shown in Fig. 3.4, the overall thermal resistance and thermal resistance of the inside of the tubes are nearly the same and decrease as the oscillation frequency increases from 6.0 to 19.3 Hz.

3.3. CORRELATIONS IN TERMS OF NONDIMENSIONAL PARAMETERS

In general, the Nusselt number for oscillating air flow is commonly thought to be influenced by the Reynolds number, Re, and the kinetic Reynolds number parameter, Re_ω, as reported in works by Tang and Cheng, Bouvier *et al.*, and N. Chen and F. Griffin [11], [15], [4]. From a statistical analysis of nonlinear fits of these parameters to the Nu_i values, it was found that only one of these parameters was necessary to sufficiently explain the variance in the Nusselt number.

In order to determine correlations for the Nusselt number, three suspect nondimensional parameters were initially involved in a factor analysis. These nondimensional parameters were: Re, Re_ω, and Pr for air. The corresponding values for these nondimensional parameters were entered into STATISTICA (a powerful statistical analysis software program) to determine the eigenvalues for the four factors (including Nu) using the method of principal components to extract the nondimensional parameters that account for the most variance in the dependent variable, Nu [25]. By using principal components, the total variability in a component is considered in the analysis (rather than using only the variability in one component which is common to other components) [25]. By inspection of eigenvalues obtained by this method and their relation to the percent of total variance, it was found that if only the first two factors were extracted (Nu and Re_ω) they would account for 95% of the cumulative variance [25]. If the additional factor, Re, was also extracted, it would correspond to just under 5% of the remaining cumulative variance, leaving the contribution of Pr to the cumulative variance negligible [25]. The decision on the number of factors to extract is at the discretion of the author, but one criterion that will be used, the scree test, has been proven through practice [25]. In the scree test, the eigenvalues are plotted as a function of the various factors considered in the analysis [25]. Factors

to the right of the interval where the curve levels-off sharply are eliminated [25]. This can be seen with eigenvalues for the nondimensional parameters as shown in Fig. 3.5.
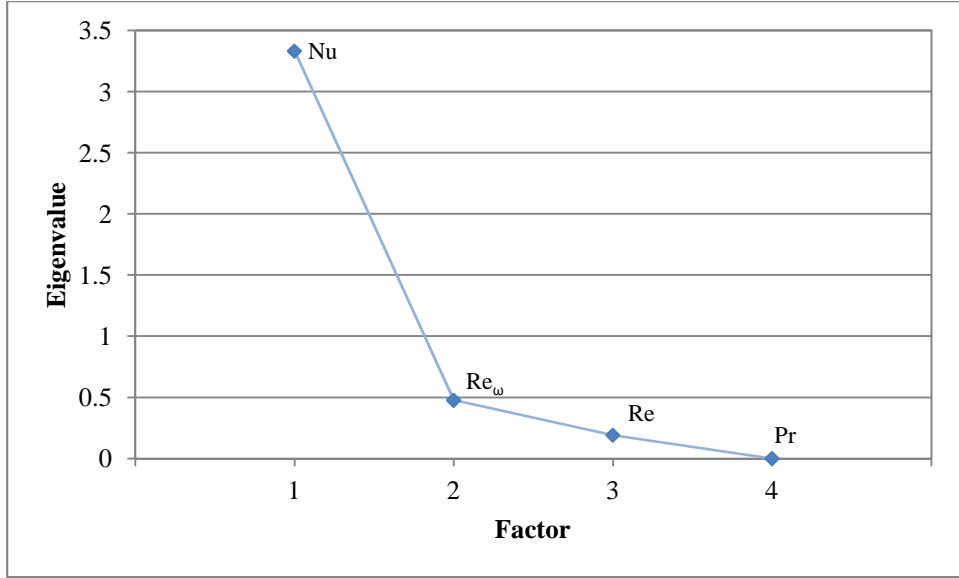

Fig. 3.5. Scree plot of eigenvalues

Fig. 3.5 suggests that only factor 1, Nu, and factor 2, Re_ω, should be extracted for the subsequent analysis since Re borders the region at which random error takes a more significant effect on the data [25]. STATISTICA is then used to correlate the Nusselt number in terms of a power equation which yielded the best least-squares fit with the kinetic Reynolds number. This correlation is presented in (29):

$$Nu_i = 0.70 \, Re_\omega^{0.47} \tag{29}$$

where Nu_i is the Nusselt number on the inside of the tubes. Generally, the Nusselt number is presented in terms of multiple nondimensional parameters such as both Re and Re_ω, but in the present research, both Re and Re_ω show equally-strong correlations with Nu to the point where the extraction of an additional parameter for (29) does not yield appreciable improvement to the correlation. This is due to the fact that data entered into both of the variables Re and Re_ω were derived from the same sources. For instance, by inspection of (18)–(21), it can be seen that the

only directly-measured data from the present experiment that factored into the calculation of Re

and Re_ω was the oscillation frequency. All other variables in these equations were based on either

the measured oscillation frequency, or on fluid properties determined with Engineering Equation

Software at the corresponding, measured air temperatures.

The correlation between Nu_i and Re_ω in (29) can be viewed in Fig. 3.6.
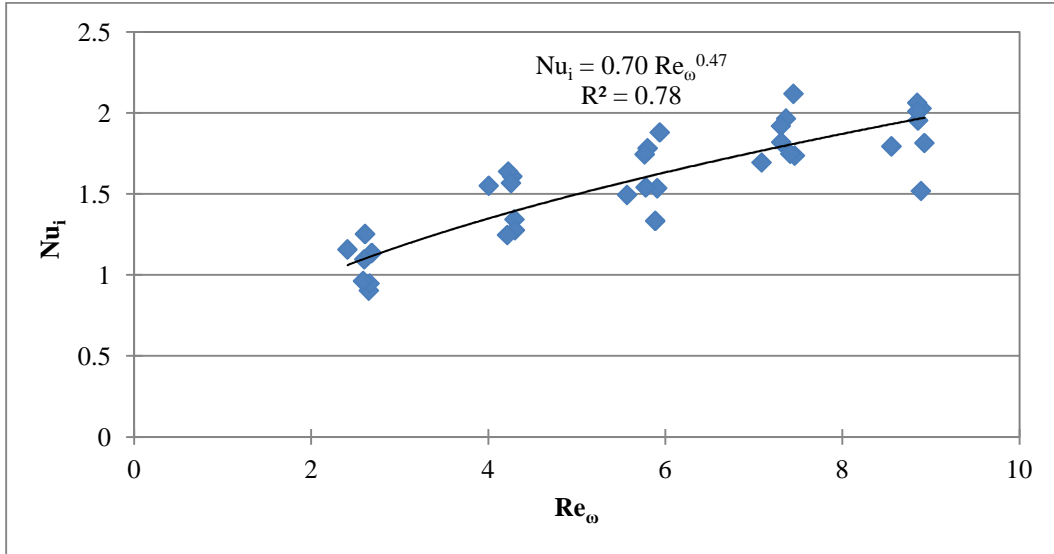

Fig. 3.6. Correlation between Nusselt and Reynolds numbers

The correlation presented in (29) demonstrates an R-squared value, R^2, of 0.78 and a standard

error, σ, of 0.18 based on the regression. As a reference, the most accurate correlation would yield

a standard error of 0 and R-squared value of 1 [11]. Note that these values were found using data

from 35 tests with 1 independent variable and 1 dependent variable. Fig. 3.7 shows the measured

Nusselt number compared to the predicted Nusselt number from an analysis performed in
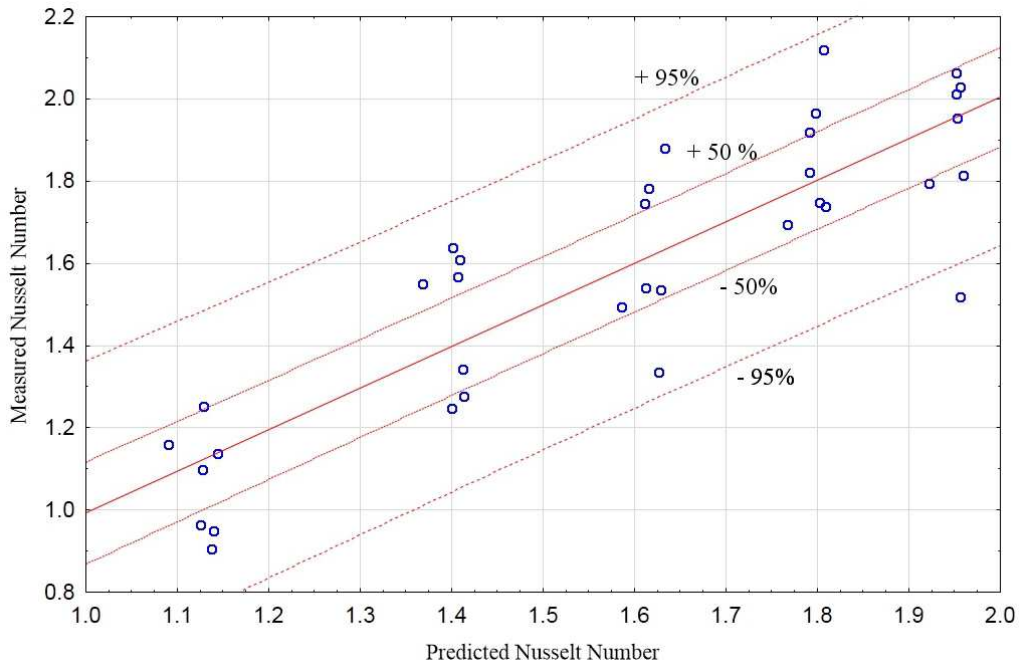
STATISTICA.

Fig. 3.7. Measured Nusselt number compared to predicted Nusselt number

The 50% and 95% confidence bands in Fig. 3.7 represent the confidence intervals of the predicted (rather than measured) values.

3.4. COMPARISON TO OTHER METHODS

In order to compare the present data to Zhao and Cheng's correlation for the space-time averaged Nusselt number in turbulent and periodically reversing air flow, the present data need to be adapted into the form of Zhao and Cheng's correlation in (23) [10]. The data obtained are plotted in Fig. 3.8.
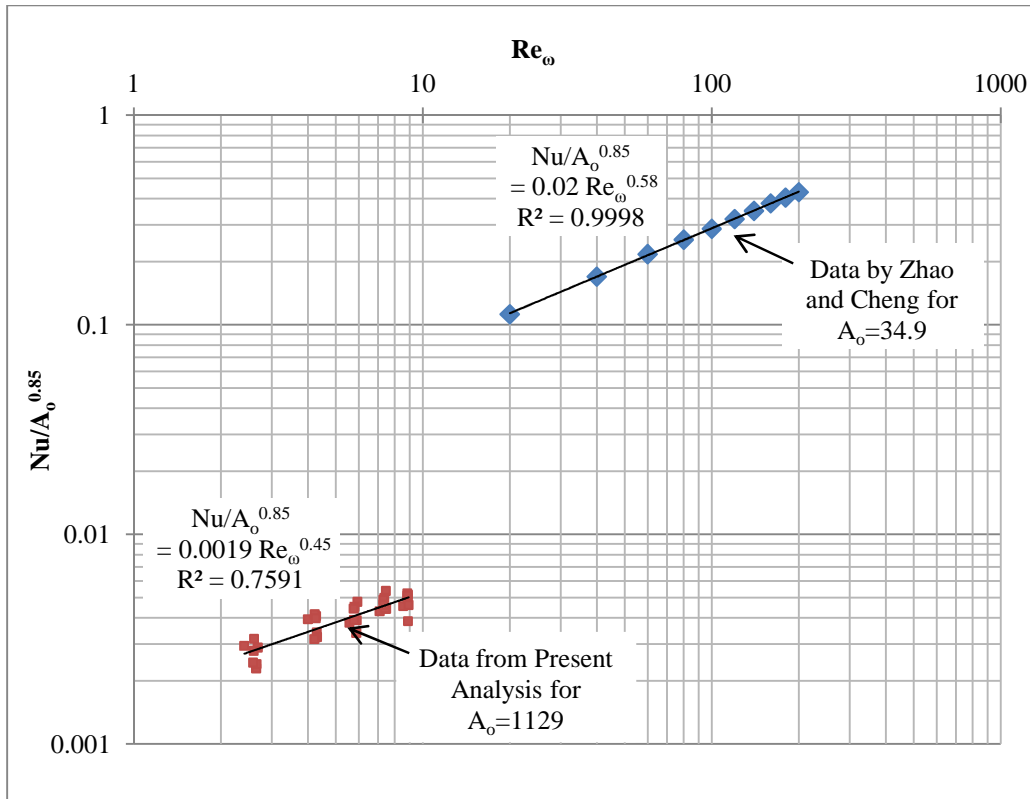
Fig. 3.8. Comparison of present data to data collected by Zhao and Cheng [10]

Fig. 3.8 indicates that the present data have a coefficient that is significantly less than the

coefficient obtained by Zhao and Cheng [10]. This fact is due to the extremely high value of A_ω

for the present data which was 1129 when compared with Zhao and Cheng's A_ω values which

ranged from 8 to 35 (although Fig. 3.8 only shows data obtained at A_ω=34.9) [10]. The exponent

of 0.58 on the kinetic Reynolds number of Zhao and Cheng's data is also higher than the 0.45

exponent on the present data; however the values are comparable [10]. The differences in the

trend lines between data sets may be due to many differences in the geometry and physical setup

of the experiments. For instance, Zhao and Cheng's experiments were performed on a single,

externally heated pipe with laminar air flow whereas the present experiment involves heat transfer

in the opposite direction (from the air to the tube walls) [10]. As noted previously, the flow

regime in the present experiment is transitional and turbulent which should have the effect of

increasing the Nusselt number on the inside of the heat exchange tubes since the Nusselt number

is proportional to the inside heat transfer coefficient. However, this is not the case as shown in

Fig. 3.8 and leads to some uncertainty in whether the definition of A_ω in (5) is appropriate for the

present experiment. Without further studies, the effect of flow regime on the differences between

the two experiments cannot be determined.

Chapter 4: CONCLUSIONS

This research contributes additional experimental data to the under-researched field of oscillatory flow heat exchange in Stirling engine coolers. A method of determining the inside, outside, and overall heat transfer coefficients is presented which yields results with reasonable trends. The outside heat transfer coefficients were found to be significantly higher than the inside heat transfer coefficients, ranging from 768 to 787 W m^{-2} K^{-1}, while the inside heat transfer coefficients ranged from 26 to 49 W m^{-2} K^{-1}. This study also details the design and development of a heat exchanger test apparatus as well as the effective measures taken to minimize external heat inputs and the impacts of electrical noise on the data.

Significant results from this study include: 1) the overall heat transfer coefficient increases as a function of increasing oscillation frequency from 21.5 to 46.1 W m^{-2} K^{-1} and is independent of heat rate; 2) the Nusselt number for the inside of the tubes is a strong function of the kinetic Reynolds number and a nondimensional correlation is provided in (29); and 3) the test apparatus has been successful throughout its design and development due to the minimization of error in the data obtained.

Although there were no experimental data from similar experiments to compare to, the comparison between the present data and Zhao and Cheng's correlation is reasonable and the differences can be easily explained by geometrical differences in the test setup [10].

Chapter 5: FUTURE WORK

   To produce the most meaningful data, various tube bundle geometries should be tested with a wider range of input heat rates. This would allow for more opportunities to scale data obtained from the test apparatus to Stirling engines currently in use. From the beginning, the heat exchanger test apparatus was designed to be adaptable to testing a wide variety of coolers and other heat exchangers, such as regenerators. In future experiments, the test apparatus may be expanded to accommodate both a cooler and regenerator so that they may be tested together.

REFERENCES

[1]   G. Walker, "Design guidelines for large Stirling cryocoolers," Cryogenics, pp. 113-114, February 1983.

[2]   B. Kongtragool and S. Wongwises, "A review of solar-powered Stirling engines and low temperature differential Stirling engines," Renewable and Sustainable Energy Reviews, vol. 7, pp. 131-154, 2003.

[3]   A. J. Organ, The Regenerator and the Stirling Engine, 1st ed. UK: Harvill Press, 1997.

[4]   N. Chen and F. Griffin, "Effects of pressure-drop correlations on Stirling-engine predicted performance," in 18th Intersociety Energy Conversion Eng. Conference, Oak Ridge, TN, 1983.

[5]   I. Urieli and D. Berchowitz, Stirling cycle engine analysis. Bristol, United Kingdom: Adam Higler Ltd., 1984.

[6]   F. de Monte, G. Galli, and F. Marcotullio, "An analytical oscillating-flow thermal analysis of the heat exchangers and regenerator in Stirling machines," in Proc. of the 31st Intersociety Energy Conversion Eng. Conference (IECEC), vol. 2, August 1996, pp. 1421-1427.

[7]   W. M. Kays and A. L. London, Compact Heat Exchangers, 3rd ed., H. B. Crawford and D. Gleason, Eds. New York, NY: McGraw-Hill Book Company, 1984.

[8]   T. Zhao and P. Cheng, "A numerical solution of laminar forced convection in a heated pipe subjected to a reciprocating flow," Int. J. of Heat and Mass Transfer, vol. 38, no. 16, pp. 3011-3022, 1995.

[9]   T. W. Simon and J. R. Seume, "A survey of oscillating flow in Stirling engine heat exchangers," Univ. of Minnesota, Minneapolis, MN, NASA Contractor Rep. 182108, March 1988.

[10]   T. S. Zhao and P. Cheng, "Oscillatory heat transfer in a pipe subjected to a laminar reciprocating flow," J. of Heat Transfer, vol. 118, pp. 592-598, August 1996.

[11]   X. Tang and P. Cheng, "Correlations of the cycle-averaged Nusselt number in a periodically reversing pipe flow," Int. Commun. in Heat and Mass Transfer, vol. 20, pp. 161-172, 1993.

[12]   A. J. Organ, "The concept of 'critical length ratio' in heat exchangers for Stirling cycle machines," in 10th Intersociety Energy Conversion Eng. Conference, Piscataway, NJ, 1975, pp. 1012-1019.

[13]   W. D. Ernst and R. K. Shaltens, "Automotive Stirling engine development project," Mechanical Technology Inc., Latham, NY, MTI Report 91TR15, 1997.

[14]   STM 4-120 Product Catalog.

[15]   P. Bouvier, P. Stouffs, and J. Bardon, "Experimental study of heat transfer in oscillating flow," Int. J. of Heat and Mass Transfer, vol. 48, pp. 2473-2482, April 2005.

[16]   R. K. Shah and D. P. Sekulić, Fundamentals of Heat Exchanger Design. Hoboken, NJ: John Wiley & Sons, 2003.

[17]   K. L. Linker, D. R. Adkins, and K. S. Rawlinson, "Testing of the STM4-120 kinematic Stirling engine for solar thermal electric systems," in Proc. of the 24th Intersociety Energy Conversion Eng. Conference (IECEC), vol. 5, August 1989, pp. 2231-2236.

[18]   E. F. Eppard, "Study of Cross-flow, Counterflow, and Parallel Flow Cooling Effects in a Stirling Engine Heat Exchanger," unpublished, undergraduate honors thesis, Barrett, The Honors College, Arizona State Univ., Tempe, AZ, 2011.

[19]   OMEGA Engineering Inc., The OMEGA Handbook Series: The Temperature Handbook, 5th ed. Stamford, CT: OMEGA Engineering Inc., 2004.

[20]   OMEGA Engineering Inc., The OMEGA Handbook Series: The Pressure and Strain Handbook, 5th ed. Stamford, CT: OMEGA Engineering Inc., 2010.

[21]   Dwyer Instruments, Inc., Bulletin No. H-11: Air Velocities with the Dwyer Pitot Tube, 1992, User Manual.

[22]   R. J. Moffat, "Using uncertainty analysis in the planning of an experiment," ASME J. of Fluids Eng., vol. 107, pp. 173-178, June 1985.

[23]   Y. A. Cengel, Heat and Mass Transfer, 3rd ed., B. Stenquist, Ed. New York, NY: McGraw-Hill, 2007.

[24]   W. A. Khan, J. R. Culham, and M. M. Yovanovich, "Convection heat transfer from tube banks in crossflow: analytical approach," Int. J. of Heat and Mass Transfer, vol. 49, pp. 4831-4838, 2006.

[25]   StatSoft, Inc. (2011) StatSoft Electronic Statistics Textbook. Tulsa, OK. http://www.statsoft.com/textbook/.

APPENDIX A

ENGINEERING EQUATION SOLVER CODE

The following Engineering Equation Solver (EES) code was used as a convenient way of determining fluid properties at the temperatures and pressures used during the experiments. Three cycles of data sampled at 1000 Hz at each frequency and heat rate were imported into EES using lookup tables and then averaged to yield the average cycle temperatures. A sample of code taken for 6 Hz (360 RPM) at a heat rate of 201 W is shown below.

```
 P_ambient=101.325;
"Approximate dewpoint temperature"
DP=(5/9)*(25-32)
"Geometric properties"
V_a_disp=(((pi*(65/2)^2)*50)/1e9)
d_h=0.049*0.0254
d_o=0.083*0.0254
A_avg=((97*pi*(d_o)*0.1314)+(97*pi*(d_h)*0.1314))/2
d_avg=(d_h+d_o)/2
A_in=(97*pi*(d_h)*0.1314); A_out=(97*pi*(d_o)*0.1314); L=0.1314
t_w=0.017*0.0254
x_max=1.406
L_d_ratio=L/d_h
d_L_ratio=d_h/L
A_f_CR=(0.1314*1.7*0.0254)-(0.1314*11*0.0254*0.083)
A_CR=(L*1.7*0.0254)-(L*11*0.0254*0.083)
"Oscillation rate"
Period_CR_[1]=(360/60)^(-1)
Frequency_[1]=1/Period_CR_[1]
"Temperatures measured with thermocouples"
T_ca_avg_CR_[1]=avgLookup ('T4 360', 'T_ca', 1, 494)
T_ha_avg_CR_[1]=avgLookup ('T4 360', 'T_ha', 1, 494)
```

T_a_avg_CR_[1]=(T_ca_avg_CR_[1]+T_ha_avg_CR_[1])/2

T_cw_CR_[1]=26.27

T_dw_avg_CR_[1]=avgLookup ('T4 360', 'T_dw', 1, 494)

T_hw_CR_[1]=T_cw_CR_[1]+abs(T_dw_avg_CR_[1])

T_w_avg_CR_[1]=(T_cw_CR_[1]+T_hw_CR_[1])/2

"Air Properties"

P_a_avg_CR_[1]=P_ambient

k_a_CR_[1]=Conductivity(AirH2O,T=T_a_avg_CR_[1], D=DP, P=14.65)

"Heat rate transferred to the water"

cp_w_CR_[1]=Cp(Water,T=T_w_avg_CR_[1],P=P_ambient)

rho_w_CR_[1]=Density(Water,T=T_w_avg_CR_[1],P=P_ambient)

m_dot_w_CR_[1]=(2.5e-005*rho_w_CR_[1])/11

q_w_eqlty_CR_[1]=(m_dot_w_CR_[1]*cp_w_CR_[1])*(T_hw_CR_[1]-T_cw_CR_[1])

"Overall heat transfer coefficient"

Delta_T1[1]=(T_ha_avg_CR_[1]-T_hw_CR_[1])

Delta_T2[1]=(T_ca_avg_CR_[1]-T_cw_CR_[1])

T_lm_CR_[1]=(Delta_T1[1]-Delta_T2[1])/ln(Delta_T1[1]/Delta_T2[1])

U[1]=q_w_eqlty_CR_[1]/(A_avg* T_lm_CR_[1])

"Outside heat transfer coefficient"

x_l=0.00274

p_t=0.00316

sc_t=p_t/d_avg

sc_l=x_l/d_avg

C_Khan=(0.61*sc_t^0.091*sc_l^0.053)/(1-2*exp(-1.09*sc_l))

mu_w_CR_[1]=Viscosity(Water,T=T_w_avg_CR_[1],P=P_ambient)

u_max[1]=rho_w_CR_[1]/(m_dot_w_CR_[1]*A_f_CR)

V_max[1]=m_dot_w_CR_[1]/(rho_w_CR_[1]*A_CR)

Re_w[1]=(rho_w_CR_[1]*d_o*V_max[1])/mu_w_CR_[1]

Pr_w[1]=Prandtl(Water,T=T_w_avg_CR_[1],P=P_ambient)

Nuss_o[1]=C_Khan*(Re_w[1])^(1/2)*(Pr_w[1])^(1/3)

k_w_CR_[1]=Conductivity(Water,T= T_w_avg_CR_[1], P=P_ambient)

h_o[1]=(C_Khan*(Re_w[1])^(1/2)*(Pr_w[1])^(1/3)*k_w_CR_[1])/d_o

"Inside heat transfer coefficient"

h_a[1]=(-1*k_w_CR_[1]*h_o[1]*U[1])/(h_o[1]*t_w*U[1]+k_w_CR_[1]*(U[1]-h_o[1]));

"Comparison to method by Zhao and Cheng"

Nuss_Zhao[1]=(h_a[1]*d_h/k_a_CR_[1])

rho_a_avg_CR_[1]=(Density(AirH2O,T=T_ha_avg_CR_[1],D=DP,P=P_a_avg_CR_[1])+Density

(AirH2O,T=T_ca_avg_CR_[1],D=DP,P=P_a_avg_CR_[1]))/2

mu_a_CR_[1]=((Viscosity(AirH2O,T=T_ha_avg_CR_[1],D=DP,P=P_ambient))+(Viscosity(AirH

2O,T=T_ca_avg_CR_[1],D=DP,P=P_ambient)))/2

nu_a_CR_[1]=(mu_a_CR_[1])/(rho_a_avg_CR_[1])

Re_omega_X_[1]=(2*pi*Frequency_[1]*d_h^2)/(nu_a_CR_[1])